Einstein centennial review article / Article de synthèse commémoratif du centenaire de l'année miraculeuse d'Einstein

The propagation of powerful femtosecond laser pulses in optical media: physics, applications, and new challenges[1,2]

S.L. Chin, S.A. Hosseini, W. Liu, Q. Luo, F. Théberge, N. Aközbek, A. Becker, V.P. Kandidov, O.G. Kosareva, and H. Schroeder

Received 8 February 2005. Accepted 21 July 2005. Published on the NRC Research Press Web site at http://cjp.nrc.ca/ on 23 August 2005.

This paper is dedicated to the late Dr. Charles (Chuck) M. Bowden, leader of the Quantum Optics Theory Group, U.S. Army Aviation & Missile Research, Development, & Engineering Center, Redstone Arsenal, Alabama, USA. Chuck had the acute foresightedness in taking the leadership to foster, support and actively encourage the international collaboration among us resulting in a much better understanding of the physics of propagation of intense femtosecond laser pulses in all optical media. In particular, our collective effort shows that national boundaries disappear when it comes to sincere collaboration. This is human.

S.L. Chin,[3] S.A. Hosseini, W. Liu, Q. Luo, and F. Théberge. Centre d'Optique, Photonique et Laser (COPL) & Département de Physique, de Génie Physique et d'Optique, Université Laval, Québec, QC G1K 7P4, Canada.
N. Aközbek. Time Domain Corp., Cummings Research Park, 7057 Old Madison Pike, Suite 250, Huntsville, AL 35806, USA.
A. Becker. Max Planck Institute for the Physics of Complex Systems, Dresden, Germany.
V.P. Kandidov and O.G. Kosareva. International Laser Center, Department of Physics, Moscow State University, Moscow, Russia.
H. Schroeder. Max Planck Institute for Quantum Optics, Garching, Germany.

[1]This article is one of a series of invited papers that will be published during the year in celebration of the World Year of Physics 2005 — WYP2005.

[2]This work is partially based upon the following paper written at the popular level: S.L. Chin. *The physics and the challenge of the propagation of powerful femtosecond laser pulses in optical media*. Phys. Canada, **60**, 273 (2004).

[3]Corresponding author (e-mail: slchin@phy.ulaval.ca).

 doi: 10.1139/P05-048

Abstract: When a powerful femtosecond laser pulse propagates in an optical medium, self-focusing occurs. Normally, it is the most powerful part (slice) of the pulse that self-focuses first during its propagation. Self-focusing is balanced by the creation of plasma in the self-focal volume, which defocuses the pulse. This balance leads to a limitation of the peak intensity (intensity clamping). The series of self-foci from different slices of the front part of the pulse give rise to the perception of a so-called filament. The back part of the pulse undergoes self-phase modulation and self-steepening resulting in a strong spectral broadening. The final pulse is a white-light laser pulse (supercontinuum). The physics of such (long distance) filamentation and the self-transformation process are reviewed both in air and in condensed matters. The self-transformation leads to a shorter pulse and is currently being studied for efficient pulse compression to the single and (or) few-cycle level. The efficient generation of a third harmonic in the filament is due to a new phenomenon called self-phase locking. The potential applications in atmospheric sensing and lightning control will be briefly discussed. The capability of melting glass leading to index change will be underlined. The paper will end with an outlook into the future of the field.

PACS Nos.: 42.65, 42.65Jx, 42.25, 42.79Qx

Résumé : Lorsqu'un puissant pulse laser femtoseconde se propage dans un milieu optique, nous observons de l'auto-focalisation. Normalement, c'est la tranche du pulse la plus puissante qui s'auto-focalise la première pendant la propagation. L'auto-focalisation est balancée par la création de plasma dans le volume d'auto-focalisation, ce qui défocalise le pulse. Un équilibre s'installe qui mène à une limitation de l'intensité du pic (auto-verrouillage). La séquence d'auto-focalisation par les différentes tranches du pulse donne naissance à la perception d'un phénomène baptisé *filamentation*. La partie arrière du pulse subit une auto-modulation de phase et une auto-élévation, résultant en un important élargissement spectral. Nous passons en revue ici la physique de cette filamentation (à longue distance et le mécanisme d'auto-transformation, dans l'air et dans une matière condensée. L'auto-transformation mène à un pulse plus court et est présentement sous étude comme moyen efficace de compression pour un pulse d'un ou de quelques cycles. La génération efficace de troisième harmonique dans le filament est due à un nouveau phénomène appelé auto-verropuillage de phase. Nous discutons brièvement certaines applications possibles, comme le contrôle de la foudre et la sonde de l'atmosphère. Nous soulignons la possibilité de la fonte du verre (milieu optique), menant à des changement d'indice. La papier conclut avec une prospective d'avenir du domaine.

[Traduit par la Rédaction]

1. Introduction

This is a review paper with an historical perspective on the development of a branch of the physics of nonlinear propagation of powerful femtosecond laser pulses in optical media (gases and condensed matters). This subject is currently an interesting topic of research at the forefront of applied physics with a lot of potential challenging physics and applications. Fundamentally, the physics of filamentation is based upon Kerr self-focusing. The phenomenon of Kerr self-focusing dates back to the 1960s [1, 2], filamentation and spectral (red) broadening were observed by Reintjes et al. [3], while the limitation of the laser intensity at the self-focus (intensity clamping) in glass was proposed in the 1970s [4]. So now, what is really new that makes it so interesting? It is the femtosecond laser pulse, being very short and powerful, it makes a huge difference. Optical breakdown (a collisional process) resulting in the total ionization of the interaction zone in the medium (see, for example, ref. 5 and references therein) could not be induced to its completion by such short pulses even in condensed matters. In the 1960s and 1970s, laser-induced breakdown with "long" laser pulses (nanosecond down to tens of

picoseconds) masked many interesting filamentation phenomena that were not even foreseen at that time. Nowadays, powerful femtosecond laser pulses can self-focus and propagate over a long distance in air in the form of an **apparent** long filament [6] whose length might probably reach many kilometres [7]. This phenomenon encompasses what was more recently known as supercontinuum generation (see, for example, ref. 8 and references therein). A new interest in understanding this phenomenon was thus rekindled. The consequence of the propagation in an optical medium is the self-transformation of the femtosecond laser pulse into a chirped white-light laser pulse [9, 10]. Application into long-range atmospheric sensing using the white-light laser pulse has been carried out [11]. One could take advantage of the temporal deformation to compress the pulse into a few energetic cycle pulses [12]. This might make the experimental work on studying intense few-cycle laser physics much easier.

We shall review the current understanding of propagation of femtosecond laser pulses in optical media and discuss the potential applications in atmospheric sensing, lightning control, material processing, third harmonic generation, etc. It will end with an look at the challenges ahead. Some new data and new physical thoughts related to some known phenomena are also included. The paper emphasizes the physics of the problem while Sect. 4 and 8.1 give the detailed theories of the propagation in gases and in condensed matters. Hopefully, this will satisfy different tastes among the readers. For the specialists who already know the problem very well, we invite them to jump to the (last) Sect. 12 where we talk about the challenges ahead of us.

2. Universality and manifestation in various optical media

The physics of filamentation is universal and occurs in all transparent media (gases, liquids, and solids). In this paper, the results of the propagation of the very popular Ti-sapphire laser will be discussed. After propagating through an optical medium, a femtosecond (fs) Ti-sapphire laser pulse (at around 800 nm) turns into a white-light pulse whose transverse pattern shows a central white spot surrounded by colored rings. The only difference is that the length of the filament is different in different media while the free-electron generation mechanisms are different between gases and condensed matters. Figure 1*a* shows a typical transverse pattern of a 5 mJ/45fs Ti-sapphire laser pulse after propagating through 25 m in air without external focusing. The colors are real.

In this paper, the filamentation processes in air, liquid, and solid together with some new unexpected phenomena and some challenging applications will be discussed. The new phenomenon includes the observation of gain in the nitrogen molecular spectra from inside filaments in air and self-phase locking of the third harmonic with the pump.

3. Propagation in air

The physics of propagation in air will be described followed by a discussion of a few challenging applications. This physics is basically the same as that in condensed matters.

3.1. Physics of filamentation

In atmospheric air, the length of a filament could be more than a 100 m long [13–15] if not kilometres [7, 16] and the ultimate length is a current challenge of experimental measurement and theoretical prediction [14]. Figure 2 shows a picture taken with an ICCD (intensified CCD) camera from the side of the filament, which is the result of the propagation of a 45 fs Ti-sapphire laser pulse in air in a clean laboratory environment. The fine line of light comes mainly from the fluorescence of nitrogen molecules [17–19] with nonuniform intensity along the propagation axis. The diameter of the line is less than 100 μm. This is a manifestation of a **single filament**; but the line is not uniform. It shows a series of brighter sections separated by darker zones. This is a manifestation that the laser pulse undergoes multiple re-focusing generating a few filaments along the same propagation axis. This observation of a line (filament) is also a possible source of debate in developing a physical picture of filamentation.

Fig. 1. (*a*) A chirped white-light laser pattern. It started from a 5 mJ/45 fs Ti-sapphire laser pulse (at around 800 nm). After propagating a distance of 25 m in air, it turns into a white-light laser pulse. Note the central white spot and the rainbow colored rings extending from red (longer wavelength) near the center to blue (shorter wavelength) at the outside. (*b*) Burn pattern of a "filament". (*c*) Conical emission from a piece of 7 mm thick BK7 glass using a sub-terawatt 800 nm, 45 fs laser pulse without external focusing.

(a)

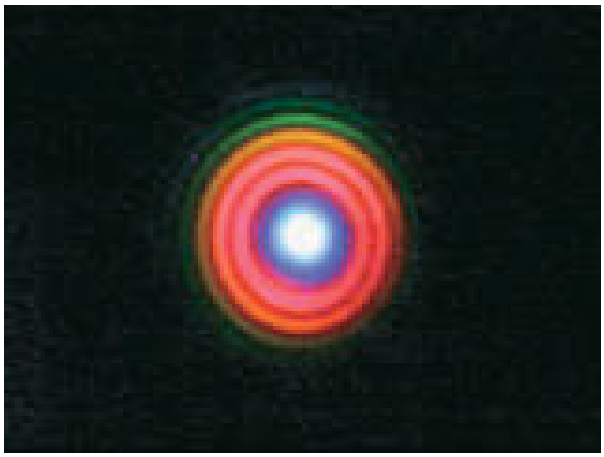

(b)

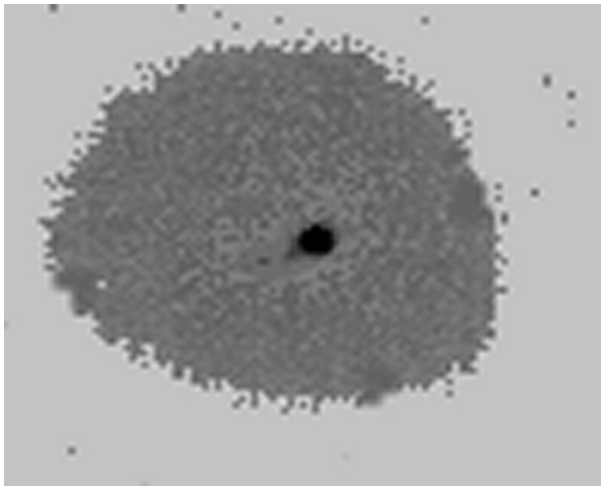

(c)

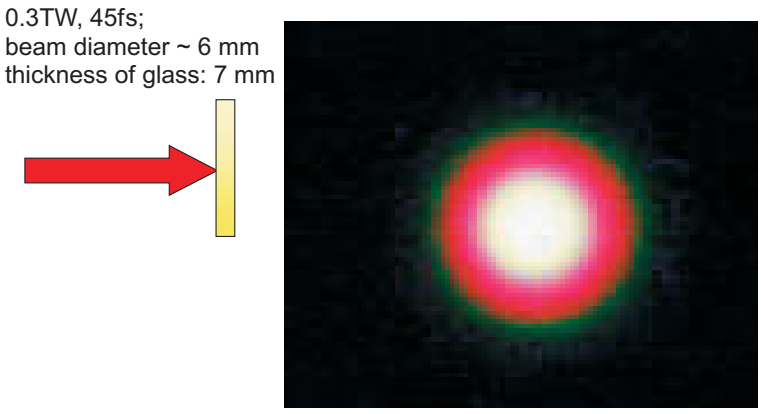

Fig. 2. Filament measured in air using an ICCD camera. The filament is produced after a $f = 5$ m focusing lens. The wavelength of the Ti-sapphire laser pulse was centered around 800 nm; the pulse energy was 13 mJ; the transform limited pulse length was 45 fs (FWHM). The diameter of the filament is of the order of 100 μm.

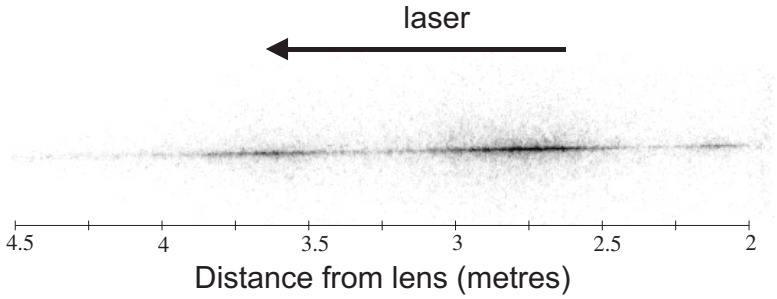

This is because if we use a sensitive burn paper to intercept the pulse at different positions of propagation, we shall observe a pattern similar to the one shown in Fig. 1*b*. The central black spot is the so-called self-focal spot and the succession of such spots (self-foci) along the propagation axis gives rise to the **perception** of a filament. Because inside this hot spot, the intensity is high (about 5×10^{13} W/cm^2; see ref. 20), nitrogen molecules are tunnel ionized. Tunnel ionization and multiphoton ionization are highly nonlinear processes that can be observed only at high laser intensities (see, for example, ref. 21 and references therein). Thus, the low-intensity pedestal outside the hot spot would **not** give rise to any measurable ionization signal. After the laser pulse has passed, the ionized molecules in the series of hot spots (self-foci) relax through collisions and fluoresce, giving rise to the picture shown in Fig. 2. It looks as if there were only a single filament (a series of hot spots) along the propagation axis; but in fact, there is a lot more radiation energy stored in the surrounding area that is normally not observed or omitted in many experiments. We call this surrounding zone the **background reservoir** [10, 22–24]. Its existence was noticed in the first demonstrations of filamentation in air [6, 25, 26] and was first interpreted in computer simulations as a background energy reservoir of the filament core [22, 23].

To describe the basic physics of filamentation (see, for example, refs. 9, 26, and 27), we consider first a collimated laser pulse with a transverse Gaussian distribution in intensity propagating in an optical medium. The central part of the pulse having a high intensity will give rise to an additional intensity-dependent nonlinear Kerr index of refraction $\Delta n = n_2 I$ (where n_2 is the second-order nonlinear index coefficient and I is the the intensity). Here, we consider only the third-order nonlinear susceptibility that gives rise to n_2. In most nonresonant optical material, this nonlinear index of refraction is positive. Hence, the total index of refraction at the central part of the pulse is higher than that at the outer zone. The velocity of propagation being c/n (where c is the velocity of light in vacuum and n the total index of refraction: $n = n_0 + \Delta n$, n_0 being the linear index of refraction), the central part of the beam will propagate at a slower velocity than in the outer zone. Thus, the wave front of the pulse will curve forward (concave) as it propagates; i.e., it is focusing more and more strongly during the propagation. This is called self-focusing. In principle, so long as there is a nonuniform intensity distribution in the wave front of the pulse, and the peak power is high enough, self-focusing will occur.

Self-focusing is a threshold process. If the peak power of a continuous wave (CW) Gaussian laser beam is higher than the critical power P_c for self-focusing, where [28]

$$P_c = \frac{3.77\lambda^2}{8\pi n_0 n_2} \tag{1}$$

the laser beam will start to self-focus. In (1), λ is the wavelength. This is the so-called whole-beam steady-state Kerr self-focusing. However, in the case of a powerful femtosecond laser pulse, both

experiment (Fig. 2 and ref. 26) and theory (see, for example, ref. 10 and references therein) show that whole-beam self-focusing does not properly describe what is happening. It is what we call "slice-by-slice" self-focusing (moving focus model) that is taking place during the propagation. The temporal shape of the laser pulse is considered to be an intensity or power envelope defined by the Poynting vector. It is visualized as subdivided into many thin intensity or power slices in time (or in space along the propagation axis). We assume that the pulse is Gaussian in space, transverse to the propagation axis z and in time (i.e., in the propagation direction), and its peak power is much higher than the critical power for self-focusing. The central slice at the peak of the pulse will self-focus at a distance z_f from the beginning of the propagation in the medium given by [28]

$$z_f = \frac{0.367ka_0^2}{\left\{\left[\left(\frac{P}{P_c}\right)^{1/2} - 0.852\right]^2 - 0.0219\right\}^{1/2}} \tag{2}$$

as if this slice were a CW beam. In (2), k and a_0 are the wave number and the radius of the beam profile at the $1/e$ level of intensity, respectively, and P is the peak power of the slice. The most powerful slice at the center of the pulse will self-focus first. As this slice self-focuses, its intensity becomes higher. Before the slice self-focuses towards a singularity, the intensity is already high enough to partially tunnel-ionize the air molecules. The resulting weak plasma density ($\sim 10^{14}$ to 10^{16} cm^{-3}) [13, 17, 29–31] would be sufficient to defocus the focusing slice back to the remaining part of the pulse or background reservoir. The highest intensity that this self-focusing slice would reach is thus limited because of the balance between self-focusing in the neutral and self-defocusing in the self-generated weak plasma. It is a constant that depends on the material property; i.e., it depends on how easy or difficult it is to generate free electrons in the self-focal zone. In air, it is around 5×10^{13} W/cm^2. We call this intensity clamping [20, 32, 33]. The energy in the defocusing slice would be reduced a little due to the loss in ionization. After passing through the self-focus, the central slice is returned (defocused) back to the remaining part of the whole pulse or **background reservoir** [22–24].

The slice in the front of the central slice would then self-focus at a later position in the propagation direction according to (2) because its peak power is lower than that of the central slice. It will undergo the same processes, namely, self-focusing, intensity clamping, and defocusing and will return the (slightly lowered) energy back to the background reservoir; and so on for successive front slices whose peak powers are higher than the critical power. Thus, the front part of the pulse would become thinner and thinner as the pulse propagates. (See Fig. 3, which is a schematic mental visualization of the deformation of the pulse as it propagates. Fujimoto et al. [34] have taken some pictures of the pulses in flight in air confirming the mental visualization of Fig. 3.) The back slices symmetrical to the front slices would, in principle, also self-focus at a position slightly behind the self-foci of the front slices. However, this would never happen because it would encounter the plasma left behind by the central and successive front slices. These back slices would thus self-focus into and interact with the plasma giving rise to a complex intensity distribution [35]. In general, the energy in the back part of the pulse would still be confined inside the highly deformed body of the pulse.

During the propagation, the repeated processes of Kerr self-focusing in the neutral gas and self-defocusing in the self-generated weak plasma of the various slices in the front part of the pulse result in an extended series of hot spots along the propagation axis; i.e., filamentation [22, 26, 36, 37]. Since the energy loss in the ionization process is small, the pulse could repeat the whole process again resulting in what we call‘ ‘self refocusing" [22, 38]. This succession of filaments is manifested by the successive sections of bright lines in Fig. 2. We call this single filamentation. The transverse pattern of the pulse measured on a sensitive burn paper at any position of propagation would be similar to that shown in Fig. 1*b*. This picture illustrates the so-called background energy reservoir first pointed out by Moloney's group [22, 23].

Fig. 3. A schematic diagram of the evolution of a femtosecond laser pulse propagating in an optical medium. The direction of propagation is towards the right-hand side. The pulse is represented by the ellipse at the left. The width of the ellipse represents the pulse's spatial width (c times the pulse length). This width is of the order of 30 μm for a 100 fs pulse; hence, a sheet of light. As such, the ellipse could be imagined as a "pancake" of light with a lot of photons inside. The central slice of the pulse self-focuses to a small area where the resulting high intensity ionizes the air molecules (star). The front part keeps on self-focusing becoming thinner and thinner. The back part encounters the plasma left behind by the front part and undergoes self-phase modulation; the resultant intensity (field) distribution becomes nonuniform and is represented by the diverging "splashes" of elongated "sub-pancakes" of light. At the end of the propagation, the pulse degenerates into a colorful white-light laser pulse.

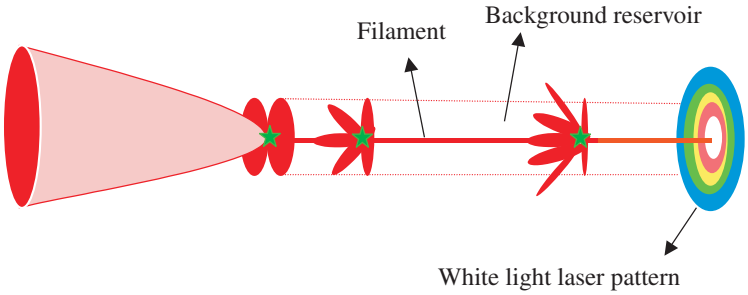

It should be emphasized here that intensity clamping sets an upper limit to the intensity at the self-focus not only in air but also in all optical media. Even if one tries to focus the pulse, so long as the focal length is not too short [39], self-focusing will always start before the geometrical focus. Thus, the intensity at the geometrical focus is either lower than or as high as that inside the self-focal zone in air. The consequence of this intensity clamping is far reaching. In air, one could have self-focusing at a long distance but one could not increase the intensity inside the self-focus even by significantly increasing of the energy of the pulse to many times the critical power; there would only be an increase of the number of self-foci (multiple filamentation, see later) each of which would have similar peak intensity. On the other hand, if the beam profile would be so smooth that only a single filament would persist while the peak power is increased significantly to many times the critical power for self-focusing, the diameter and hence the volume of the filament would increase while the intensity inside this larger volume would still be clamped. In practice, this would be a tough condition to fulfill because any little fluctuation in intensity on the beam profile would lead to self-focusing so long as the local power is higher than the critical power for self-focusing.

In many experiments, an external lens is used to force self-focusing within the limited length of the medium. Self-focusing is then reinforced by the external lens such that the self-focus appears before the position of the geometrical focus. The new self-focusing distance z_f' satisfies the lens transformation equation: $1/z_f + 1/f = 1/z_f'$ where z_f is the self-focusing distance given by (2) and f is the geometrical focal length of the lens [40]. Figure 4 [39] shows the measured fluorescence from nitrogen molecules from inside the filament regions using three different focal lengths. Figure 4*a*, for long geometrical focal length, filamentation occurs before the geometrical focus while the intensity at the geometrical focus is low. Figure 4*b* when the geometrical focal length becomes shorter, the filament ends into the geometrical focus. Figure 4*c* self-focusing and geometrical focusing become indistinguishable when the geometrical focal length is very short. However, if the power of the pulse is further increased, re-focusing will again show up giving rise to a filament after the geometrical focus (see Fig. 16 and the discussion therein).

3.1.1. Experimental proof of the existence of background reservoir

An experiment was performed to confirm directly the existence of the background reservoir [41]. If this idea were right, blocking the background and letting the central filament (hot spot) to pass through

Fig. 4. The competition between self-focusing and geometrical focusing in air. Images show the measured fluorescence from nitrogen molecules from inside the weak plasma regions. They are taken via a grating's zeroth-order image; the 42 fs laser pulse propagates towards the top; input energy, 5 mJ/pulse. (*a*) $f = 100$ cm, (*b*) $f = 30$ cm, and (*c*) $f = 5$ cm; inset: low-contrast pictures of $f = 30$ cm and $f = 5$ cm. (*a*) When the geometrical focal length is long, filamentation occurs before the geometrical focus. (*b*) When the geometrical focal length becomes shorter, the filament ends into the geometrical focus. (*c*) Self-focusing and geometrical focusing become indistinguishable when the geometrical focal length is very short.

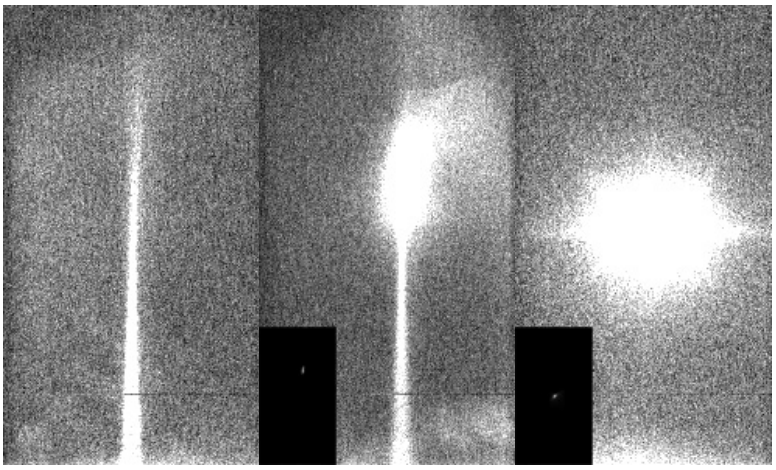

a pinhole would immediately stop filamentation after the pinhole. Figure 5 shows the result of imaging the filament in air after letting the filament punch a pinhole through an aluminum foil. Figure 5*a* shows the full filament (nitrogen fluorescence) when the aluminum foil was absent. Introducing the aluminum foil into the filament and letting it punch a hole through the foil, the tail part of the filament disappears immediately (Fig. 5*b*), indicating that the filament cannot survive without the background reservoir. (The arrow points at the scattering of the laser light by the pinhole. The insert of Fig. 5*b* shows the damaged holes on the aluminum foil after multiple shots. They are not uniform because of both beam wandering and the occurrence of multiple filaments.)

Other papers also showed the existence of the background reservoir using other approaches. Brodeur et al. [26] measured the energy of a filament that passed through a hole of 400 μm diameter (about four times larger than the filament diameter) and found only roughly 10% of the total energy of the pulse. Courvoisier et al. [42] used various types of pure water and opaque liquid droplets of up to 95 μm in size to block the filament of about 150 μm in diameter. They still found a refocusing of the pulse and filamentation beyond this blockage.

3.2. White-light laser (or supercontinuum generation)

The interaction of the high intensity in the self-focal regions with the neutral gas and with the plasma results in the modulation of the phase of the pulse; i.e., self-phase modulation (SPM) (see for example, ref. 27). The consequence is spectral broadening towards both the red and the blue sides. SPM in an optical medium is caused by the temporal variation of the refractive index. In the plane-wave approximation, the plane-wave front at the self-focus is given by the function

$$F(z, t) = \exp\{i\,[\omega_0 t - kz]\} = \exp\left\{i\left[\omega_0 t - \frac{\omega_0 n}{c} z\right]\right\} \tag{3}$$

where z is the propagation distance and ω_0 is the central angular frequency of the laser.

$$n \cong n_0 + \Delta n\,(t) \tag{4}$$

Fig. 5. Images of the filaments (due to nitrogen fluorescence) (*a*) without pinhole and (*b*) with pinhole intercepting the filament. The sudden disappearance of the filament before the pinhole is artificial. The CCD camera was set at an angle from a distance downstream of the pulse propagation towards the filament zone including the foil. Thus, the foil would block the field of view partially resulting in the sudden disappearance of the filament in front of the foil. The arrow points at the scattering of the laser light by the back part of the pinhole. The insert in *b* shows the damaged holes on the aluminum foil after multiple shots. They are not uniform because of both beam wandering and the occurrence of multiple filaments.

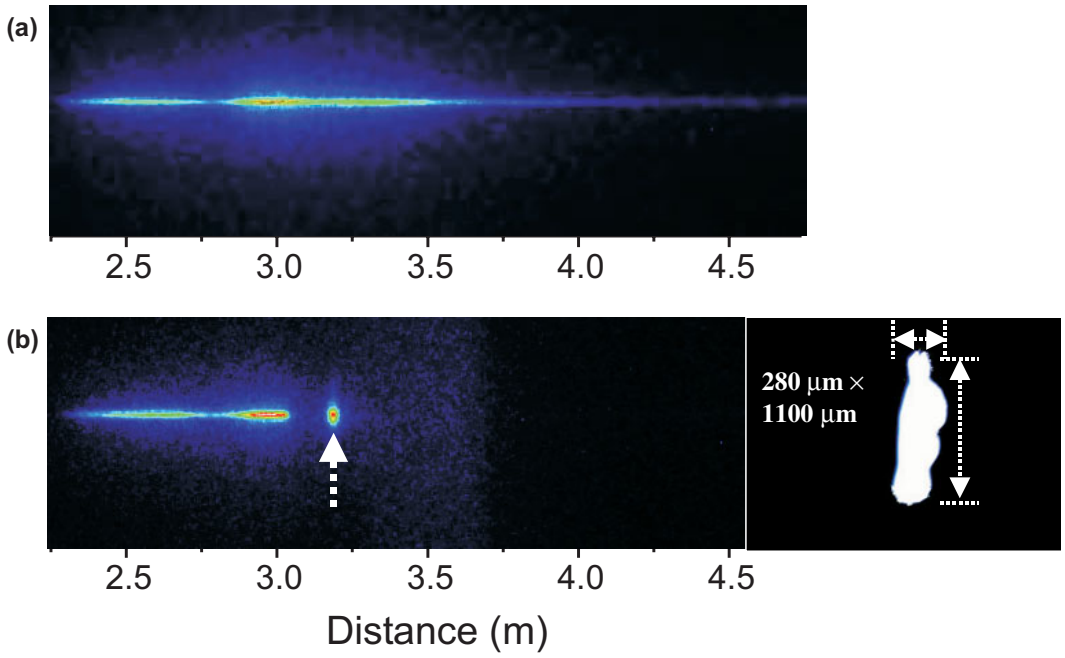

$$\Delta n\,(t) = n_2 I\,(t) - \frac{4\pi e^2 N_{\rm e}(t)}{2m_{\rm e}\omega_0^2} \tag{5a}$$

Here, $n_2 I\,(t)$ is the Kerr nonlinear refractive index of the neutral gas, $I\,(t)$ is the intensity. The last term is the plasma contribution where $N_{\rm e}(t)$ is the electron density generated through tunnel ionization of the molecules; e and $m_{\rm e}$ are the charge and mass of an electron, respectively. We note that the electron–ion recombination time is normally of the order of many nanoseconds, much longer than the femtosecond time scale of the pulse. Hence, the generated plasma could be considered as static during the interaction with the pulse.

The wave enters the optical medium at ($z = 0$, $t = 0$). At the position z, (3) becomes

$$F(z,t) = \exp\left\{i\left[\omega_0 t - \frac{\omega_0 n_0}{c}z - \frac{\omega_0 \Delta n\,(t)}{c}z\right]\right\} \tag{5b}$$

$$= \exp\left\{i\left[\left(\omega_0 t - \frac{\omega_0 n_0}{c}z\right) + \int_0^t \frac{\partial}{\partial t}\left(-\frac{\omega_0 \Delta n\,(t)}{c}z\right)\,{\rm d}t\right]\right\} \tag{5c}$$

$$\equiv \exp\left\{i\left[\left(\omega_0 t - \frac{\omega_0 n_0}{c}z\right) + \int_0^t (\Delta\omega)\,{\rm d}t\right]\right\} \tag{5d}$$

where

$$\Delta\omega = \frac{\partial}{\partial t}\left(-\frac{\omega_0 \Delta n\,(t)}{c} z\right) = -\frac{\omega_0}{c} z \frac{\partial[\Delta n\,(t)]}{\partial t} \tag{6}$$

SPM is the modulation (variation) of the phase of the wave due to the self-generated extra phase $-(\omega_0 \Delta n\,(t)/c)z$ (see (5b)). It is manifested by the frequency shift $\Delta\omega$ of (5d) and (6). Since the front part of the pulse always sees a neutral gas, from (6) and (5), without the plasma contribution,

$$\Delta\omega = -\frac{\omega_0 z}{c}\frac{\partial[\Delta n\,(t)]}{\partial t} = -\frac{\omega_0 z}{c} n_2 \frac{\partial I(\text{front part})}{\partial t} < 0 \tag{7}$$

The last inequality in (7) arises because the front part of the pulse has a positive temporal slope whose value ranges continuously between zero and a maximum value; hence, the front part of the pulse contributes principally to red (Stokes) shift and (or) broadening. But the back part of the pulse should also see the neutral gas since the gas is only partially ionized. SPM in the neutral gas would lead to a blue shift and (or) broadening but this blue shift is masked by the stronger blue shift and (or) broadening due to SPM in the plasma together with the eventual SPM due to the very steep descent of the back part of the pulse (i.e., self-steepening [43, 44]).

The contribution of the plasma term in (5) to frequency shift and (or) broadening starts soon after the plasma is generated. The plasma interacts at the self-focal zone with the self-focusing slice of the pulse and with the slices coming from behind (i.e., from the back part of the pulse). Using (5) and (6), the frequency shift and (or) broadening due to the plasma term is

$$\Delta\omega = +\frac{2\pi z e^2}{c m_\mathrm{e} \omega_0}\frac{\partial N_\mathrm{e}}{\partial t} \tag{8}$$

The electrons are generated through tunnel ionization of the air molecules. For simplicity, we can use the experimental results to empirically state that the effective tunnel ionization rate of nitrogen (and oxygen) molecules is proportional to the intensity raised to the power of m where m is the empirical slope of the experimental ion yield versus intensity curve in the log–log scale [45]. Thus, the electron density can be expressed as [33]

$$N_\mathrm{e} \cong N_0 w \int_{-\infty}^{t} I^m(t)\,\mathrm{d}t \tag{9}$$

In (9) N_0 is the density of the neutral air, w is the effective empirical tunnel-ionization rate of nitrogen (and oxygen) and I^m is the empirical power law of the ionization. Substituting (9) into (8), we obtain

$$\Delta\omega = +\frac{2\pi z e^2 N_0 w}{c m_\mathrm{e} \omega_0} I^m(t) \tag{10}$$

This positive blue shift and (or) broadening of the frequency is large partially because of the highly nonlinear dependence on the high intensity inside the self-focal region.

Besides SPM, towards the end of the propagation; i.e., towards the end of the diffraction length given by ka^2 (k is the wave number and a, the beam radius at $1/e$ value), the back part of the intensity distribution of the pulse becomes very steep and **the slope is negative**. This temporal variation happens mostly in the neutral gas because it is at the end of filamentation where ionization is negligible. It would give rise to a large blue shift of the frequency since by analogy to (7)

$$\Delta\omega = -\frac{\omega_0 z}{c} n_2 \frac{\partial I(\text{very steep back part with negative slope})}{\partial t} \tag{11}$$

Fig. 6. Illustration of the various wave vectors of a spherical wave front in the self-focal region. (*a*) All the possible wave vectors in the propagation z-direction are shown. (*b*) Illustrating the transverse part of the wave vector.

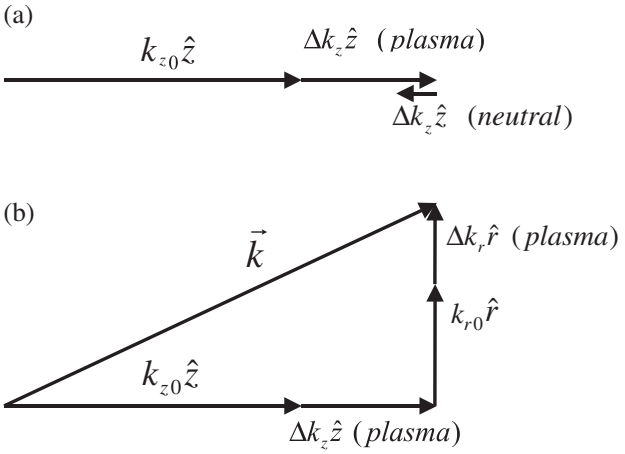

This is a major source of the large broadening towards the blue side of the pump frequency. This so-called self-steepening in the case of the propagation of a powerful femtosecond pulse is the consequence of a continuous spatio-temporal self-transformation process of the pulse during propagation. Numerical simulation (see Sect. 4) will give a quantitative picture of what happens [43, 44]. Here, we will give a very qualitative, simple-minded picture so as to grasp a physical feeling of self-steepening. Group-velocity dispersion and the interaction with the plasma are neglected. The central slice of the pulse with the highest intensity where ionization occurs would propagate with a velocity c/n where $n = n_0 + \Delta n_{\mathrm{Kerr}} - \Delta n_{\mathrm{p}}$. Here, n, is the total index of refraction, n_0, Δn_{Kerr}, and Δn_{p} are the indices of refraction of the neutral air, the nonlinear Kerr index, and the index of the plasma, respectively. At the intensity clamping position, $\Delta n_{\mathrm{p}} = \Delta n_{\mathrm{Kerr}} = n_2 I$. This focusing central slice with intensity clamping would thus have an index of refraction $n_{\mathrm{c}} = n_0$; it would propagate faster than the front part of the pulse, which sees an increase of the index of refraction due to the nonlinear contribution (Kerr nonlinear index) only $n_{\mathrm{f}} = n_0 + \Delta n_{\mathrm{Kerr}}$; i.e., no plasma generation yet. Now the back part of the pulse sees a weak plasma generated by the peak of the pulse. The index of refraction of this plasma zone is the combined values of the neutral and the weak plasma; i.e., $n_{\mathrm{b}} = n_0 + (\Delta n_{\mathrm{Kerr}})_{\mathrm{b}} - \Delta n_{\mathrm{p}}$; here $(\Delta n_{\mathrm{Kerr}})_{\mathrm{b}} < \Delta n_{\mathrm{p}}$ because the intensity of this back slice is weaker than the clamped intensity while the plasma is left behind by the clamped intensity. Hence, $n_{\mathrm{b}} < n_{\mathrm{c}} < n_{\mathrm{f}}$; i.e., the back part of the pulse would propagate faster than the front part of the pulse. Soon, the back part would almost catch up with the front part resulting in a steep rise in intensity at the back part. SPM is proportional to the derivative of this part of the pulse; hence, a very large blue shift according to (11).

The propagation distance z also plays a role in both the red and blue broadening (see (7) and (10)); thus, during experimental observations, the spectral broadening of the pulse develops progressively as the propagation distance increases. Both experiment and numerical simulation [10, 43, 44, 46] show similar broadening. A strong broadening in air towards the red up to 4 μm was recently reported [47]. The central part of the pattern of Fig. 1 is an example of such frequency broadening from the pump at 800 nm towards the blue side across the whole visible frequency range; hence, it appears white. This is what we call the self-transformed white-light laser pulse.

3.3. Conical emission

The colorful rings in Fig. 1*a* are another manifestation of self-phase modulation in the radial direction (conical emission; for a general review, see also ref. 27). The previous section describes self-phase

modulation in the plane-wave approximation; i.e., in the z-direction only. That is to say, we have considered only the wave vector k_z. However, the laser pulse front is curved at the self-focal zone. It contains a transverse part of the wave vector. In a normally spherically symmetric pulse front, the general wave vector $\boldsymbol{k}$ is given by

$$\boldsymbol{k} = k_z\hat{z} + k_r\hat{r} = k_{z0}\hat{z} + \Delta k_z\hat{z} + k_{r0}\hat{r} + \Delta k_r\hat{r} \tag{12}$$

where the initial wave vectors contain a subscript zero. $\hat{z}$ is a unit vector in the propagation direction; $\hat{r}$ is a unit vector transverse to $\hat{z}$. In the plane-wave approximation described above, we have considered only the z-components. They are

$$k_{z0}\hat{z} = \frac{\omega n_0}{c}\hat{z}$$

$$\Delta k_z\hat{z} = -\frac{\omega\Delta n}{c}\hat{z} = \int_0^t \frac{(\Delta\omega)}{z}\,\mathrm{d}t\,\hat{z} \qquad \text{(from (5b) and (5d))}$$

$$= \begin{cases} -\frac{\omega_0}{c}n_2\int_0^t \frac{\partial I(\text{front part})}{\partial t}\,\mathrm{d}t\hat{z} < 0 & \text{(in neutral gas)} \\ +\frac{2\pi e^2}{cm_e\omega_0}\int_0^t \frac{\partial N_e}{\partial t}\,\mathrm{d}t\,\hat{z} > 0 & \text{(in plasma)} \end{cases} \qquad \text{(from (7) and (8))} \tag{13}$$

$$= \begin{cases} -\frac{\omega_0}{c}n_2\int_0^z \frac{\partial I(\text{front part})}{\partial z}\,\mathrm{d}z\hat{z} < 0 & \text{(in neutral gas)} \\ +\frac{2\pi e^2}{cm_e\omega_0}\int_0^z \frac{\partial N_e}{\partial z}\,\mathrm{d}z & \hat{z} > 0\text{(in plasma)} \end{cases} \tag{14}$$

We see that from (13) and (14), the temporal rate of change has been transformed into a spatial rate of change by recognizing that $z = ct$. Figure 6*a* gives a schematic relationship of these waves vectors. $\Delta k_z\hat{z}$(plasma), being positive, is in the same direction as that of the original vector $k_{z0}\hat{z}$ while $\Delta k_z\hat{z}$ (neutral), being negative, is in the opposite direction to that of $k_{z0}\hat{z}$.

Equation 14 (together with (8)) shows that the spatial gradient of the electron density gives rise to a blue shift of the frequency in the z-direction (plane wave approximation). Since electrons are generated in the three-dimensional self-focal volume, electron density gradients show up in all directions; i.e., in both the z- and the r-directions. In the r-direction, the electron-density gradient would give rise to a spatial divergence of the radiation. Thus, the wave vector, $\Delta k_r\hat{r}$ (plasma), which is in the direction of $k_{r0}\hat{r}$, would make this blue-shifted radiation diverge into a ring as shown by the vector diagram in Fig. 6*b*. The larger the electron-density gradient is, the larger will be the wave vector $\Delta k_r\hat{r} \sim \frac{\partial N_e}{\partial r}\boldsymbol{r}$ and the blue shift ((8) and (14)). The radial electron-density gradient varies continuously from zero to a maximum value. The detailed analysis of conical emission is given in refs. 10 and 48. From Fig. 6*b*, the divergence of the resultant vector $\boldsymbol{k}$ will be larger when the electron-density gradient is larger. Hence, rainbow-type colored rings are generated around the central white spot; the larger the frequency shift is (i.e., the shorter the shifted wavelength is), the larger the divergence will be. The rings in Fig. 1 are thus explained. The frequency shift due to the neutral gas would not give rise to rings because the wave vector $\Delta k_r\hat{r}$ (neutral) points in the opposite direction to $\boldsymbol{k}_{r0}$; i.e., it tends to reduce the divergence of the wave. When the above description was done numerically in a three-dimensional calculation, the agreement between theory and experiments is excellent. Other theories, such as four-wave mixing and Cherenkov radiation have been proposed but they fail to satisfy all the experimental observations [10].

Before ending this section, we comment on the repeating dark circular rings in the conical emission (Fig. 1*a*). It is due to the spectral interference (see, for example, ref. 49) of the conical emissions coming from two to three on-axis filaments due to multiple refocusing (Fig. 2). Assume that there are two sets

of conical emissions from two re-focusing filaments along the same axis. Because each color of a conical emission is generated continuously along a filament, the width of each color on the observation screen is wide. Hence, there will be overlap of the same color coming from the two filaments. At the overlapping positions, those colors satisfying the condition $nd = (m + 1/2)\lambda$ (d = pathdifference between the conical light of the same color coming from two different filaments, λ = wavelength, n = indexofrefraction, m = integer) would give rise to destructive interference (dark rings) while those satisfying $nd = m\lambda$ would give rise to constructive interference. If there is a bunch of filaments occurring around the propagation axis, there will be so many overlapping rings that the whole conical emission becomes a blur of continuous colored bands with no dark rings. This situation can be achieved by passing a sub-terawatt pulse through a piece of BK7 glass without external focusing (Fig. 1*c*). In this case, the peak power (300 GW) is much higher than the critical power for self-focusing in glass (a few megawatts) so that multiple refocusing as well as multiple filaments occur around the propagation axis.

4. Theory

The propagation and interaction model describing the evolution of ultra-short intense optical pulses in an optical medium is an important part of the fundamental understanding of this phenomenon. Due to a number of linear and nonlinear effects such as self-focusing, dispersion, self-phase modulation, and ionization, the overall dynamics of such pulses can be complicated where both transverse and temporal effects play equally important roles [9, 23, 35, 37, 44, 50–53]. The propagation of the optical pulse is described by Maxwell's equations. However, solving Maxwell's equations directly requires enormous computational efforts and in many cases does not provide an insight to the basic physical understanding of the various linear and nonlinear effects involved. Therefore, an approximate wave equation is used instead with a more reasonable mathematical solution. The interaction of intense optical pulses in a bulk medium is highly nonlinear and the material response must, therefore, self-consistently couple with the wave equation.

From Maxwell's equations it is possible to obtain a second-order scalar wave equation for the electric field. Considering a linearly polarized electric field E, the equation reads (in Gaussian units)

$$\frac{\partial^2 E}{\partial z^2} + \frac{\partial^2 E}{\partial x^2} + \frac{\partial^2 E}{\partial y^2} - \frac{4\pi}{c^2}\frac{\partial^2 P}{\partial t^2} - \frac{4\pi}{c^2}\frac{\partial J}{\partial t} = 0 \tag{15}$$

where P is the polarization response of the medium and includes both linear and nonlinear responses of the medium. The current density J comes from free electrons created by field ionization. It can be written as

$$J = -eN_e v_e \tag{16}$$

where the electron velocity v_e is derived from

$$\frac{\partial v_e}{\partial t} = -\frac{eE}{m_e} \tag{17}$$

Let us take the time derivative of (16) and assuming that the initial electron velocity is zero when it is created, we obtain

$$\frac{\partial J}{\partial t} = \frac{e^2 N_e}{m_e} E \tag{18}$$

Inserting (18) into (15) we obtain

$$\frac{\partial^2 E}{\partial z^2} + \frac{\partial^2 E}{\partial x^2} + \frac{\partial^2 E}{\partial y^2} - \frac{4\pi}{c^2}\frac{\partial^2 P}{\partial t^2} - \frac{4\pi e^2 N_e}{c^2 m_e} E = 0 \tag{19}$$

First we consider laser pulse propagation in the frame work of the slowly varying envelope approximation (SVEA) and will discuss the effects of higher order correction terms such as self-steepening later. We assume that the medium polarization is given by $P = \chi^{(1)}E + \chi^{(3)}E^3$, where $\chi^{(1)}$ and $\chi^{(3)}$ describe the linear and nonlinear coefficient, respectively. The dielectric function is given as $\varepsilon = 1 + 4\pi\chi^{(1)}$. The electric field is assumed as a rapidly oscillating part $\exp[-i\omega t + ikz]$ that is modulated by an envelope given as $E(x, y, z, t) = \varepsilon(x, y, z, t)\exp[-i\omega t + ikz] + \text{c.c.}$, where $\varepsilon(x, y, z, t)$ is assumed to be a slowly varying envelope function such that it varies slowly in time and space on the scale of ω^{-1} and k^{-1}. Inserting P and E into (19) and applying the slowly varying envelope approximation one obtains

$$i\frac{\partial\varepsilon}{\partial z} + \frac{1}{2k}\nabla_{\perp}^2\varepsilon + n_2k_0|\varepsilon|^2\varepsilon - \frac{2\pi e^2N_e}{km_ec^2}\varepsilon + i\Gamma\varepsilon = 0 \tag{20}$$

Here, $\nabla_{\perp}^2 = (\partial^2/\partial x^2) + (\partial^2/\partial y^2)$ is the transverse Laplacian operator. In addition, for simplicity, effects arising from the group velocity dispersion are neglected and can be added easily as is done later. Equation (20) is the so-called nonlinear Schrödinger equation. The intensity of the pulse is defined as $I = |\varepsilon|^2$ given in units of W/cm^2, and $n_2 = 12\pi^2\chi^{(3)}/n_0^2c$ is the nonlinear coefficient given in units of cm^2/W, and Γ accounts for ionization losses. The generation and evolution of electron density $N_e(z, x, y, t)$ for single ionized molecules is given by

$$\frac{\partial N_e}{\partial\tau} = (N_0 - N_e)\,R\left(|\varepsilon|^2\right) \tag{21}$$

where R is the multiphoton and (or) tunnel ionization rate (in units of s^{-1}) for air molecules (oxygen and nitrogen) and N_0 is the number density of neutral molecules in units of molecules/cm^3. Effects such as electron recombination and cascade ionization are neglected as they do not play an important role for pulses shorter than one picosecond. The ionization model for oxygen and nitrogen molecules is described in the next section. To simplify the numerical simulations the rate is fitted in the form of $R = \sigma^{(n)}I^n$, where $\sigma^{(n)}$ and n are fitting parameters. When necessary a more complex fitting function is used to obtain the best fit. The ionization rates used in the calculations in ref. 54 agree well with the experimental data of ref. 45 for an 800 nm pump pulse. Since the plasma generation plays an important role in the propagation dynamics it is, therefore, crucial to use ionization rates for oxygen and nitrogen molecules that are suitable for pulse intensities and pulse width of interest.

Equation (20) when coupled to (21) includes the most basic linear and nonlinear terms for describing self-focusing, diffraction, plasma generation, and defocusing leading to the concept of laser pulse filamentation. It is referred to as the nonlinear Schrödinger equation and has been studied widely in nonlinear optics. As we will show later, the slowly varying envelope approximation breaks down but nevertheless provides an important physical understanding of this phenomenon.

As a representative example, we consider the propagation of an initially collimated Gaussian beam of the form $\varepsilon(r, \tau) = A_0\exp[-(r^2/w_0^2 + \tau^2/\tau_0^2)]$, where w_0 and τ_0 are the initial beam radius and pulse width, respectively, measured at $1/e^2$ of the intensity (Fig. 7*a*). Equations (20) and (21) are integrated with $w_0 = 0.025$ cm, $\tau_0 = 85$ fs, and $P_0 = 6P_{cr}$, where $P_{cr} = 3$ GW is the critical power for self-focusing in air at 800 nm. In addition, cylindrical symmetry of the transverse profile is assumed, which is valid when describing the evolution of a single filament.

4.1. Ionization rate model

Electron generation through multiphoton ionization of nitrogen and oxygen molecules (we assume that air is a mixture of 80% nitrogen and 20% oxygen) is taken into account via the rates R. In the nonperturbative intensity domain (above 10^{13} W/cm^2) exact calculations via ab-initio time-dependent theoretical simulations by direct solution of the quantum mechanical Schrödinger equation would require an enormous computational power and are currently limited to small one- and two-electron molecules,

Fig. 7. Shown is the spatio-temporal intensity distribution of (*a*) an initially Gaussian pulse propagating in ionizing air at (*b*) $z = 0.4$ and (*c*) $z = 0.8$. The intensity is normalized to the peak input intensity and the radius and time coordinates are scaled to the initial beam radius and pulse width, respectively.

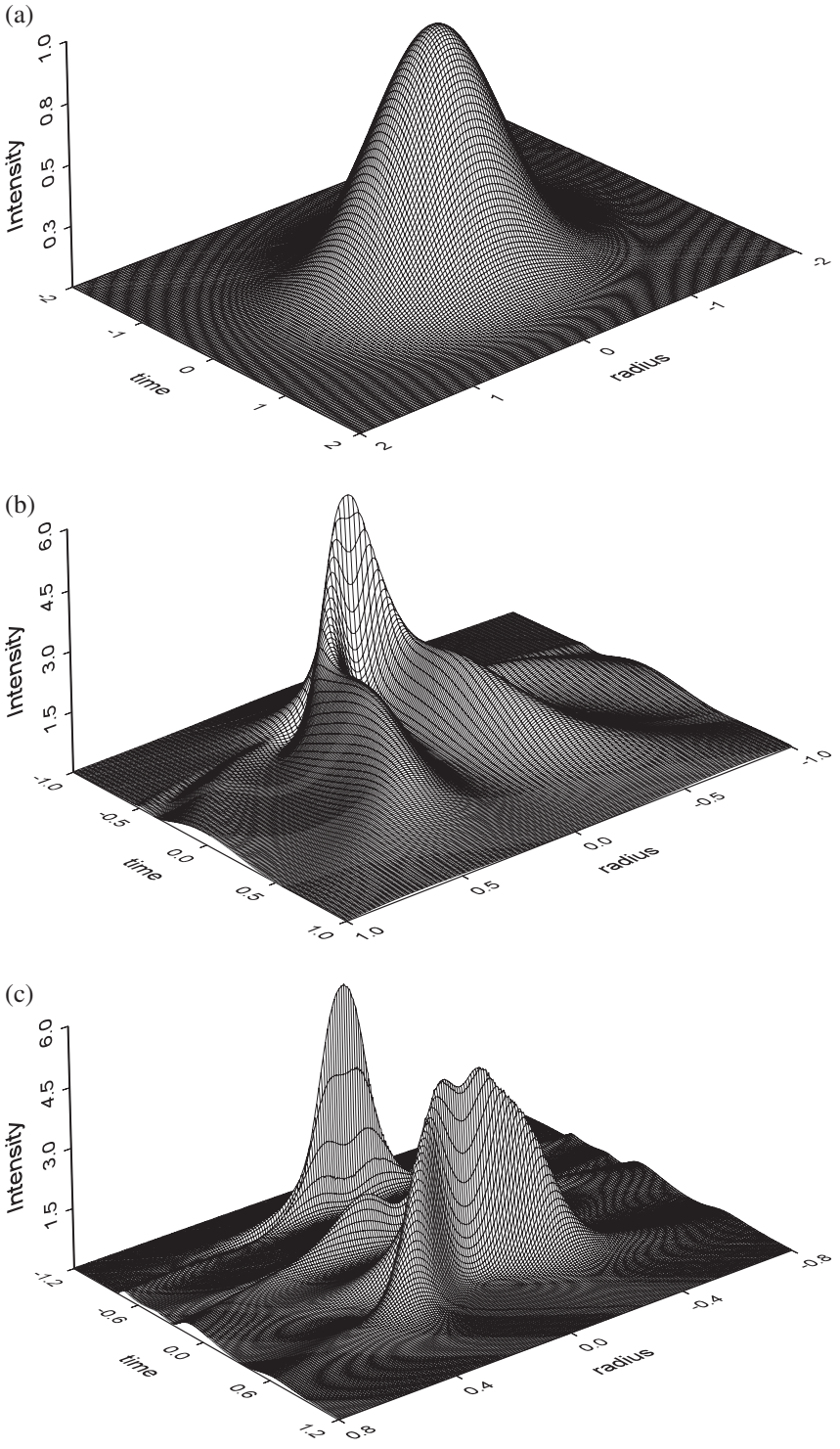

e.g., H_2^+ or H_2 (see, for example, ref. 55). An alternative approach is a systematic approximation method for intense-field problems in more complex di- or polyatomic molecules given by the Intense-Field Many-Body S-Matrix Theory (IMST), for a recent review see ref. 56). In the S-matrix theory, it is possible to incorporate (*a*) the Coulombic interactions between the charged particles in an atom or molecule and (*b*) the highly nonlinear laser interaction, which are of comparable strength, on an equal footing. The theory has been successfully applied to several intense-field single electron processes in atoms, such as above-threshold ionization and high harmonic generation, as well as to more complex systems or processes such as double and multiple ionization of two- and many-electron atoms, and ionization of di- and polyatomic molecules in intense fields [56]. An ionization rate formula for atoms [57–60] and molecules [54, 61] has been derived that is found to be in good agreement with a large number of sets of experimental data, including those for ionization of oxygen and nitrogen [45].

According to this rate formula (in Hartree atomic units; i.e., $\hbar = e = m_e = 1$), the total rate of ionization of a molecule with N_e electrons in its highest occupied molecular orbital in a linearly polarized laser field is given by

$$R(I) = 2\pi N_e \left[\frac{(2I_p)^{3/2}}{E_0}\right]^{\left(2/\sqrt{2I_p}\right)} \sum_{N=N_0}^{\infty} k_N \left(U_p - N\omega\right)^2 \int d\hat{k}_N J_N^2 \left(\boldsymbol{\alpha}_o \cdot \boldsymbol{k}_N ; \frac{U_p}{2\omega}\right) \left|\left\langle \phi_{\boldsymbol{k}_N} \phi_f^+ \middle| \phi_i \right\rangle\right|^2$$

where I_p is the ionization energy of the molecule, $J_n(a; b)$ is the generalized Bessel function of two arguments, $\alpha_0 = \sqrt{I}/\omega$ is the quiver radius and $U_p = I/4\omega^2$ is the quiver energy of an electron in the field of frequency ω and peak intensity $I = |\varepsilon|^2$, $k_N^2/2 = N\omega - U_p - I_p$ is the kinetic energy of the electron, and N_0 is the minimum number of photons needed to be absorbed from the field to ionize the molecule. It has been found, for example, in ref. 62 that for nitrogen and oxygen the experimental rates as a function of the intensity follow rather straight lines in a log–log plot of the singly charged ion yield versus intensity [45], which suggests further approximating the rates by a fit to the form $R = \sigma^{(n)}|\varepsilon|^{2n}$ for the relevant intensity range up to about 10^{14} W/cm^2. Note that the exponent n is, in general, unlike the result of multiphoton perturbation theory, not an integer number. Since this linear fit on the log–log plot follows the experimental results in ref. 45 very well, the latter results could also be used as empirical data in the numerical calculation as a first approximation. This approximation would be valid for "long" pulses because the experiments were done using 200 fs pulses. But since during filamentation, the pulse gets shorter and shorter, the interaction (ionization) physics would evolve into the few-cycle regime where the experimental results would not be the same. However, the ionization rates obtained using the IMST are still valid as long as the pulse width at half the maximum intensity (FWHM) is at least three field cycles long [60].

4.2. Refocusing phenomenon and filament formation

Figures 7*a*–7*c* give the results of simulation in which the spatio-temporal intensity distribution is plotted at a propagation distance (normalized to the diffraction length of the collimated input beam $kw_0^2/2z = 0$, $z = 0.4$, and $z = 0.8$, respectively, [44]. As the pulse self-focuses the peak intensity increases very rapidly until there is enough plasma to stop the focusing process. The strongest part of the pulse will come to a focus first followed by other parts of the pulse. This is the basis of the idea of "slice-by-slice self-focusing" as discussed qualitatively in the previous sections. The plasma generation is an accumulative process and each slice experiences a different magnitude of plasma defocusing. Thus, some of the earlier slices will reach a higher peak intensity before being defocused (intensity clamping, see description above). These time-dependent focusing and defocusing processes lead to the temporal reshaping of the pulse. As seen in Fig. 7*b* there is a sharp leading edge with a smoother and very broad back component. This latter spatially broad distribution of the field partially constitutes the background reservoir. With further propagation a second pulse appears at the back of the leading pulse, as seen in

Fig. 7*c*. The spatially broad low-energy field distribution (background reservoir) exists persistently so long as there is self-focusing.

The main physical mechanism of filament formation is due to a continuous competing effect between self-focusing and defocusing. To understand this competing mechanism further, in Fig. 8*a* we plot the filament energy, defined as the energy contained in a 150 μm diameter to the total pulse energy as a function of the propagation distance [44]. Initially due to self-focusing, more energy of the pulse is channelled into the core region until there is enough plasma generated to stop the self-focusing process, and the beam starts to defocus. However, the defocusing is stopped and the pulse refocuses again, which can be seen as the second peak in the filament energy. This process can repeat itself many times, which is apparent from Fig. 8*a* as a weak third peak in the filament energy. The multiple refocusing phenomenon was observed in the experiment (see Fig. 2 and the discussion of refocusing above), and our results are in good qualitative agreement. Figure 8*b* shows the generated electrons along the propagation direction and clearly it agrees with the refocusing discussed in the filament energy description. Whenever the pulse refocuses more electrons are being generated which are seen as the peaks in Fig. 8*b* and their location agrees well with the peaks in the filament energy depicted in Fig. 8*a*. Alternatively, one can examine each temporal slice of the temporal intensity profile as a function of propagation distance. In Fig. 8*c*, we plot the on-axis $I(r = 0, \tau = 0)$ temporal slice, which has the highest peak power. It will come to a focus first and the peak intensity increases until plasma defocusing stops the self-focusing process and it starts to defocus, but it only defocuses until self-focusing takes over again. This process can take place many times resulting in multiple self-focusing collapses. The refocusing of the pulse channels energy back into the core of the beam and thus represents the process in which energy is exchanged between the core and the outer part (reservoir) of the beam. This is one of the important physical mechanisms of the long-range propagation and filament formation in air.

More readings can be found in refs. 22, 23, 26, 35, 44, 45, and 53.

In the next section, we describe briefly how the balance between self-focusing and defocusing occurs and describe the refocusing phenomenon using a very simple model.

4.3. Variational method

As we have seen in the previous section, the dynamics of these pulses is complex due to the reshaping of the laser pulse both temporally and spatially. We have developed a variational method [35] in which a semi-analytical result can be obtained without resorting to lengthy computational simulations. Particularly, it shows explicitly how the self-focusing process is stopped by plasma defocusing and thus provides a direct physical insight to an otherwise complicated problem. The variational method is based on defining a Lagrangian functional L for the system from which (20) can be derived using $\delta L/\delta\varepsilon^* = 0$. Such an approach has been successfully implemented in a number of cases such as optical pulse propagation in optical fibers [63], self-focusing collapse [64], and optical solitary waves in a photonic band gap crystal [65].

The Lagrangian density for the nonlinear Schrödinger equation (20) without the ionization loss term is given by

$$L = \frac{i}{2}\left(\varepsilon\frac{\partial\varepsilon^*}{\partial z} - \varepsilon^*\frac{\partial\varepsilon}{\partial z}\right) + \frac{1}{2k}\left(\left|\frac{\partial\varepsilon}{\partial x}\right|^2 + \left|\frac{\partial\varepsilon}{\partial y}\right|^2\right) - \frac{\alpha}{2}|\varepsilon|^4 + \frac{\gamma}{n+1}|\varepsilon|^{2n+2} \tag{22}$$

Here, $\alpha = n_2 k$ and $\gamma = 2\pi e^2 N_0 \sigma^{(n)} \tau_0 / k m_e c^2$. In addition, the electron density is approximated as $N_e = \tau_0 N_0 \sigma^{(n)} |A|^{2n}$. It can be easily shown that (20) with $\Gamma = 0$ can be derived from

$$\frac{\delta L}{\delta\varepsilon^*} = \frac{\partial}{\partial z}\left[\frac{\partial L}{\partial\left(\partial\varepsilon^*/\partial z\right)}\right] - \frac{\partial L}{\partial\varepsilon^*} = 0 \tag{23}$$

Fig. 8. Shown (*a*) is the filament energy contained in a cylinder of 150 μm diameter and (*b*) corresponding generated electrons per length as a function of the propagation distance (normalized to the diffraction length). As the pulse self-focuses more energy is channeled into the core region in which the filament energy increases until there is sufficient plasma generated so that the pulse starts to defocus. However, the pulse refocuses again around $z = 0.55$ as seen in the second peak in (*a*). A third refocusing appears around $z = 0.8$. This refocusing is consistent with the generated electrons (*b*) in which more electrons are generated during the refocusing of the pulse. In (*c*) a particular intensity slice, $I(0, 0)$ is plotted as a function of the propagation distance.

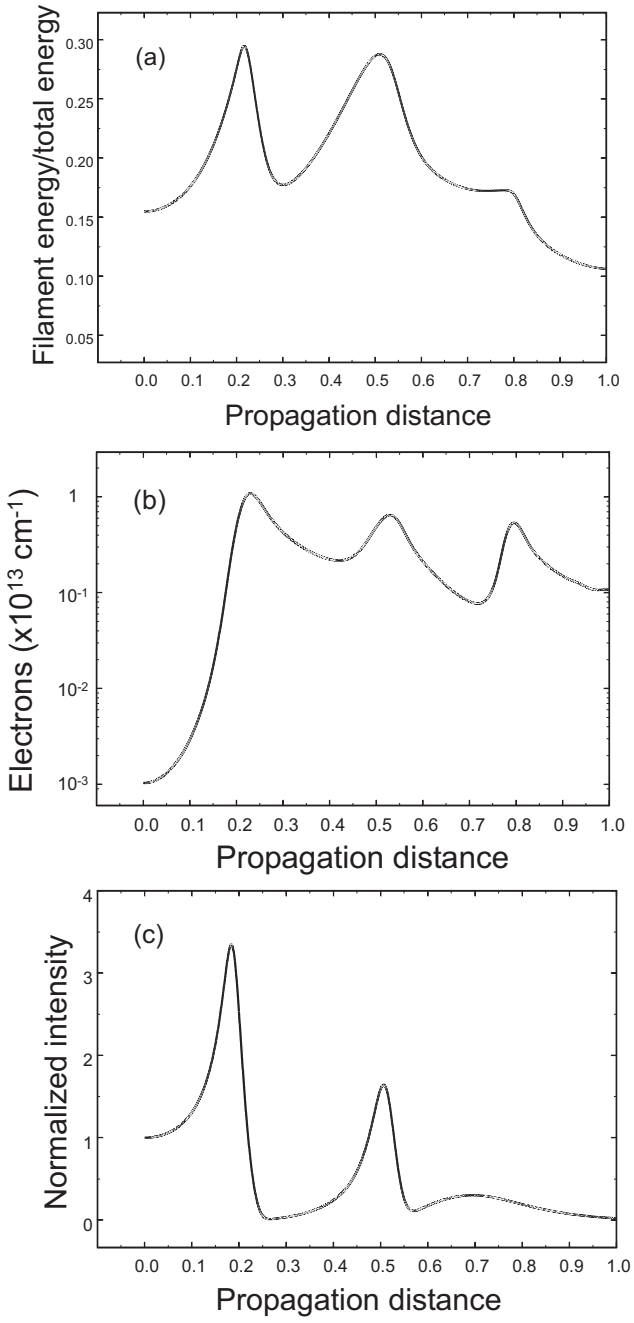

using the Lagrangian density defined in (22). We use the following trial solution for $\varepsilon(x, y, z, \tau)$:

$$\varepsilon(z, x, y, \tau) = A(z, \tau)\ \exp\left[-\frac{(x^2 + y^2)}{a^2(z, \tau)}\right] \exp[ib(z, \tau)(x^2 + y^2) + i\phi(z, \tau)] \tag{24}$$

Here A, a, b, and ϕ are variational parameters and depend both on z and τ. These variational parameters are sufficient to describe the most important features such as self-focusing, plasma defocusing, and self-phase modulation. However, it is important to note that the trial solution (24) is assumed to have a Gaussian type transverse beam profile. It is always possible to expand the envelope function in terms of a complete set of eigen functions, which would allow the study of transverse modulations such as ring formation and multiple filaments. However, our goal here is to obtain a qualitative picture as transparent as possible. Inserting the trial solution (24) into the Lagrangian density (22) and integrating over the transverse coordinate (x, y) we obtain a reduced Lagrangian $\hat{L} = \int L\,\mathrm{d}x\,\mathrm{d}y$, which depends only on the variational parameters and the independent variables z and τ. In this case, the higher dimensional problem is reduced to a one-dimensional one. A set of first-order differential equations for the variational parameters can be obtained from the equations of motion, $\partial\hat{L}_z/\partial\mu - \partial L/\partial\mu = 0$ where $\hat{L}_z = \partial\hat{L}/\partial\mu_z$ and μ represents each variational parameter. It can easily be shown that the coupled set of equations can be further reduced to a single equation for the beam radius $a(z, \tau)$,

$$\frac{1}{2}\left(\frac{\partial a}{\partial z}\right)^2 + U(a) = 0 \tag{25a}$$

and $U(a)$ is given as

$$U(a) = \frac{2}{a^2} - \frac{2P_0}{a^2} + \left[\frac{8\gamma k P_{\mathrm{cr}}^n 2^n}{2n\pi^n(n+1)(2n+2)a_0^{2n-2}}\right]\frac{P_0^n}{a^{2n}} + C \tag{25b}$$

where C is a constant of integration determined by the initial conditions. Equations (25) describe the motion of a classical particle moving in a potential well $U(a)$. Here a describes the fictitious position of the particle and z acts as fictitious time variable. The potential is shown in Fig. 9*a* for the case when the initial peak power exceeds the threshold power for self-focusing. In the absence of plasma defocusing, the particle is released from rest and since the potential diverges (dotted-line) it approaches zero, which corresponds to beam collapse, and has been studied widely. On the other hand, in the presence of plasma defocusing, self-focusing is overcome by the plasma defocusing and the particle comes to rest at a minimum beam radius, $a_{\min}$. However, it then rolls back, refocusing the beam, and reaches its initial position. Since no losses are included in the motion, it oscillates between two points in the potential creating the self-focusing and defocusing of the laser beam. This can be seen in Fig. 9*b* in which the corresponding beam radius is plotted as a function of propagation distance. This self-focusing and defocusing is in qualitative agreement with numerical results shown in Fig. 8*c* in which one particular time slice is plotted as a function of propagation direction and the competing effect between self-focusing and defocusing agrees well with the potential-well description. It is important to note that, a quantitative agreement is not expected between the numerical and variational results since in the trial solution the functional dependence of the amplitude and phase is fixed. Nevertheless, using this method we were able to study the entire pulse dynamics and obtained qualitative agreement with experimental results.

4.4. Higher order linear and nonlinear effects: Beyond the slowly varying envelope approximation

The nonlinear Schrödinger equation (20) provides a good physical insight into the mechanism of filament generation in air. However, as shown in Fig. 7, the laser pulse undergoes significant reshaping

Fig. 9. Shown are (*a*) the potential $U(a)$ in which the particle moves as a function of a (normalized to the input beam radius) and (*b*) the beam radius $a(z)$ as a function of propagation distance z. The solution corresponds to the case where the particle is released from $a = 1$ at rest. When there is no defocusing effect the potential diverges (dotted line) and the particle (open circle) rolls towards $a = 0$, i.e., the beam collapse. However, in the presence of defocusing there is significant change in which the defocusing effect becomes dominant at some position and stops the focusing (continuous line). Here, the particle (solid circle) will oscillate between two points. This oscillation manifests itself as a alternating self-focusing and defocusing of the beam radius shown in (*b*).

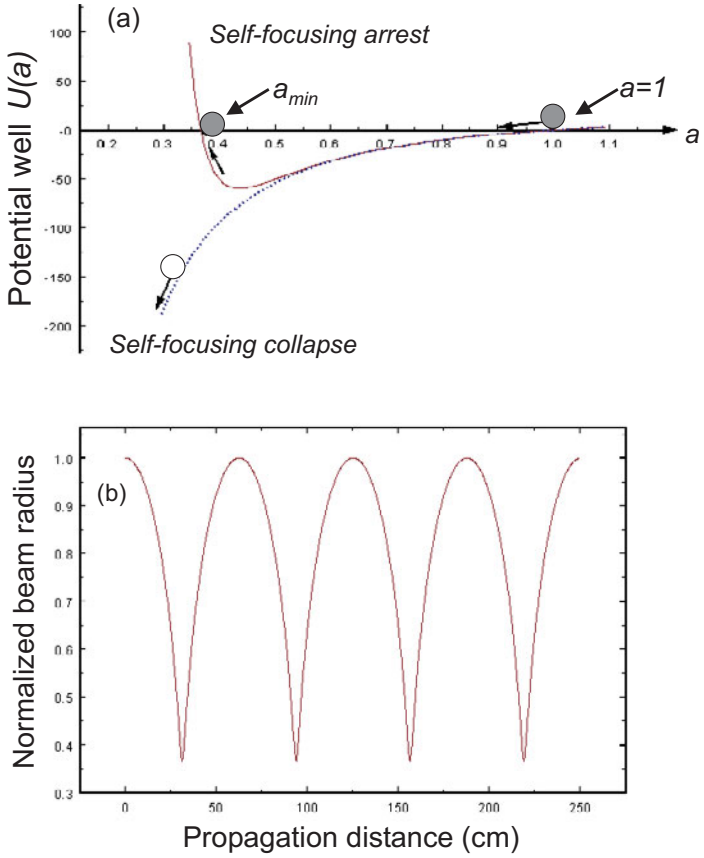

where steep edges as well as sub-pulses emerge. Under these conditions the validity of the nonlinear Schrödinger equation becomes questionable. Another important aspect is that the short sub-pulses generated during the filamentation process may be on the order of a few optical cycles. It is, therefore, apparent that a propagation model valid for few cycle pulse propagation must be adapted. However, this must be done self-consistently with the response of the medium, particularly the multiphoton and (or) tunnel ionization process. It is, therefore, important to obtain a wave equation that describes optical pulse propagation on the order of only a few cycles. Several approaches have been taken to describe few-pulse propagation but here we adapt the formalism given in ref. 66. The propagation equation is given in ref. 44

$$\left[i\frac{\partial}{\partial z} + \frac{1}{2k}\nabla_\perp^2 - \frac{k''}{2}\frac{\partial^2}{\partial \tau^2} + n_2 k_0 |\varepsilon|^2 - \frac{2\pi e^2 N_e}{k m_e c^2} + i\Gamma \right] \times \varepsilon - \frac{i}{\omega}\frac{\partial}{\partial \tau}\left(\frac{1}{2k}\nabla_\perp^2 - n_2 k_0 |\varepsilon|^2 - \frac{2\pi e^2 N_e}{k m_e c^2} \right)\varepsilon = 0 \quad (26)$$

Fig. 10. The power spectrum of the pulse at a propagation distance $z = 1.0$ (in units of diffraction length), in the case of the SVEA (dotted line) and with self-steepening effect (dotted–broken line) are compared. The continuous curve is the initial pulse spectrum at $z = 0$. It is apparent that higher order terms in (1) cause a much stronger blue shift when compared to the SVEA. The spectral intensity is normalized to the peak input spectral intensity.

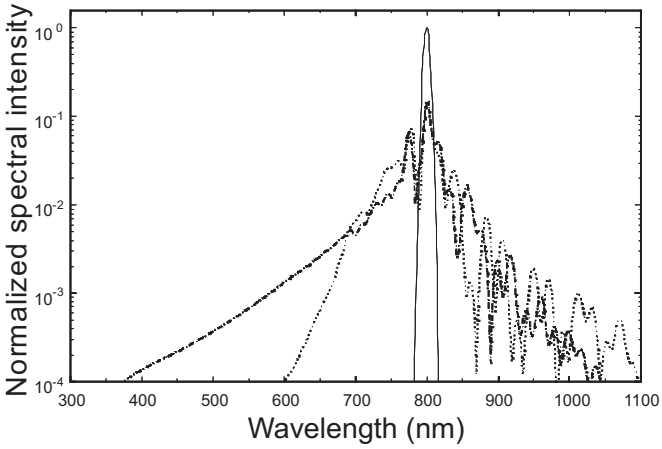

The terms in the bracket at the left side of (26) describe the slow-varying envelope approximation (SVEA) whereas those at the right side relate to higher order terms that go beyond the SVEA. Here, we also added group-velocity dispersion effects described by the parameter k''. One important higher order effect is the self-steepening effect. It is known that self-steepening of the pulse causes a sharp drop at the trailing edge of the pulse resulting in a shock formation in analogy to an acoustic wave. This can be understood by the fact that the group velocity of the pulse is intensity dependent such that the peak of the pulse travels more slowly than the wings, as described in Sect. 3.2 qualitatively. Self-steepening may have an important effect on the evolution of the pulse and in particular may cause a strong asymmetric spectral broadening. For instance, the sharp edge formed at the back of the pulse could have an important contribution to the blue extent of spectral broadening because of the strong gradient of the pulse.

To understand the effect of the self-steepening on the pulse dynamics, in Fig. 10 the pulse spectrum is shown at $z = 1.0$ in the case of the SVEA (dotted line) and with self-steepening effect (dotted–broken line). For reference the initial pulse spectrum (continuous line) is also presented. It can be seen that the self-steepening of the pulse causes a much broader blue shift [44]. This is due to the fact that a shock is formed at the back of the pulse as depicted in Fig. 11. The overall spectral shape and frequency range is in good qualitative agreement with the supercontinuum generation observed in air [7] and rare gases [67]. Although plasma defocusing contributes to the spectral broadening of the pulse spectrum, the self-steepening pushes the pulse energy further to the blue and the development of the shoulder in the spectrum is directly related to the shock formation at the trailing edge of the pulse.

As a final note, it is important to emphasize that the propagation equation derived in ref. 66 was shown to be valid even for single cycle pulses; its validity, however, must be further tested for intense pulse propagation in air. For instance, paraxial effects as well as vectorial effects [68–70] were neglected and may become important especially in the regime of multiple-filament formation. It is, therefore, important to verify the validity of the propagation equation with the solution of the full Maxwell equations. Such analysis is particularly important for the understanding of few-cycle pulse propagation and interaction in optical media. Particularly, for few-cycle pulses, the stationary response of the medium described by a constitutive relation of the polarization may no longer be valid and the full dynamics must be considered. There has been already the demonstration of few-cycle pulse generation through filamentation [12] but a rigorous theoretical modeling is still lacking.

Fig. 11. The spatio-temporal intensity profile is plotted with all higher order terms included at a propagation distance $z = 1.0$. Notice the sharp shock formation at the back of the pulse, which causes a strong blue shifting of the spectrum depicted in Fig. 10 (dotted–broken line).

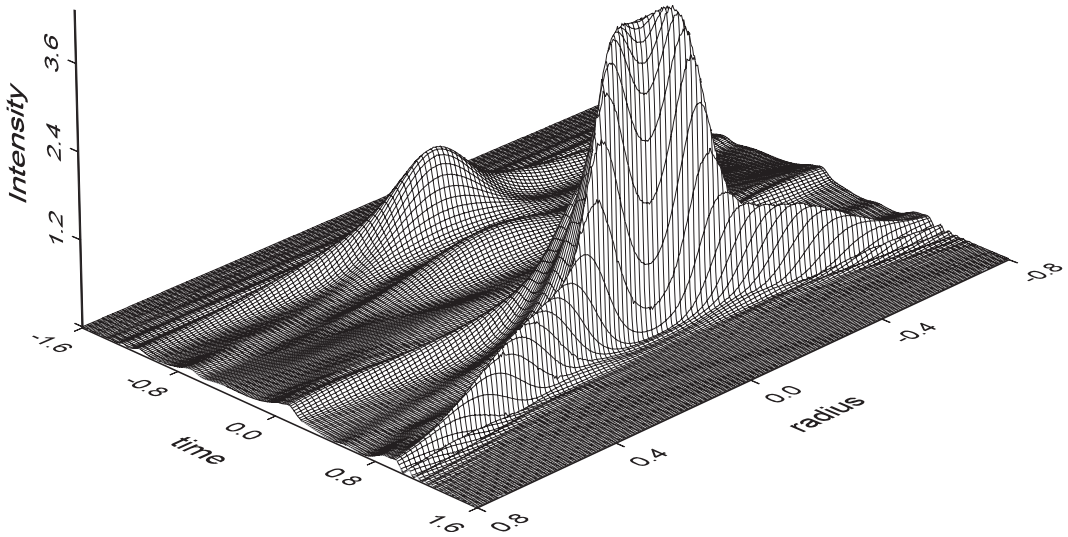

5. Multiple filamentation and filament competition

The above description pertains to a single filament arising from one higher intensity ("warm") zone of a pulse. Very often, the pulse front is not uniform either because of inherent imperfection of the laser itself or because of external perturbation such as turbulence in air (see, for example, ref. 71) or the passage through a window [72] etc. The basic principle of multiple filamentation [73] is the formation of more than one warm zone on the wave front. Each warm zone will undergo self-focusing when the pulse propagates in air as if it were an independent pulse. But these warm zones are not independent from one another because they all try to feed energy from the whole pulse's background reservoir into their own self-foci. This constitutes a competition for energy [74–76].

The underlying physics of multiple-filament competition is essentially field redistribution inside the pulse during propagation. It consists of two inter-related scenarios. One scenario is linear field interference inside the pulse during propagation and self-deformation through the optical medium. The other is nonlinear field redistribution due to nonlinear propagation effects.

In the first scenario, consider first a warm zone as being a single pulse. When a slice of the warm zone self-focuses towards a high intensity spot, tunnel ionization of air molecules occurs and the intensity is clamped. With further propagation, the slice will diverge outwards becoming a conical wave that interferes with the background field (a quasi plane wave) giving rise to concentric rings around the self-focus [72, 77]. When two adjacent warm zones self-focus into two near-by self-foci, the two sets of rings (or rather, the two conical waves and the background quasi-plane wave) will interfere giving rise to a star-like pattern [72]. This is shown in Fig. 12 in which two filaments and (or) hot spots (one strong and one weak) interfere forming such a star-like structure. Theoretical calculation based upon the above idea of the interference of conical waves and the background quasi plane wave indeed reproduces the experimental observation [72]. When more than two near-by filaments interfere, the resultant field would give rise to more complicated structures with more new warm zones that would undergo self-focusing again during further propagation. New "children" filaments are thus formed at new positions both along the propagation axis and on the cross sectional surface [74, 75].

However, if the warm zones or filaments are far apart, interference would be too weak to form new and sufficiently warm zones for self-focusing. This would constitute the second scenario in which the

Fig. 12. Interference of two filaments one weak, one strong.

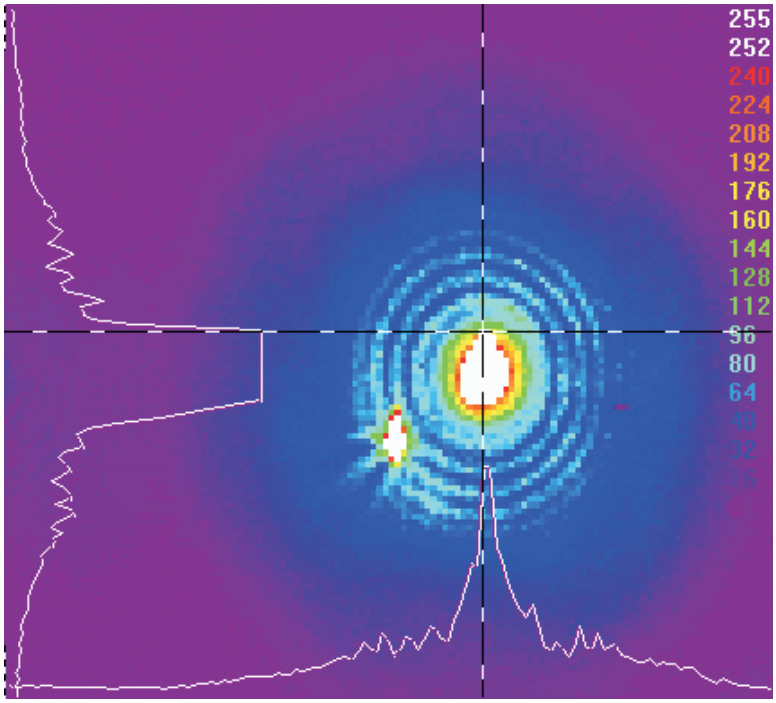

initial warm zones would each go its own way as if they were independent. During the propagation, the nonlinear self-focusing effect would help each of the warm zones to "pull" the field towards its own self-focus as if each filament "sucks" energy from the background reservoir. The consequence of this competition for energy from the same background reservoir would be such that the filaments do not have enough energy to develop fully into self-steepening.

Such competition for energy would also take place in the first scenario with filaments adjacent to one another but in a more constructive way because the filaments are close to one another. Apart from creating children filaments, the central bunch of filaments would collectively suck energy from the background reservoir towards them as if they were one single filament. The consequence of this latter case is that all these filaments become mature almost at the same time over a short distance of propagation. In air, in such a short distance, the nitrogen fluorescence signal is very strong. After this short distance, the children filaments take over but will not be as strong as before [75].

These two scenarios were observed in our recent experiments [74, 75]. We measured the nitrogen back-scattered fluorescence from long filaments in air using a LIDAR (laser radar) technique. We found that with a beam diameter of about 25 mm ($1/e^2$ of fluence) over which the multiple warm zones were sufficiently far apart, the back-scattered fluorescence from the generated multiple filaments had a huge fluctuation. For the same input laser peak power of about 1 TW (1 TW = 10^{12} W), the fluorescence signal sometimes came from the full propagation length of 100 m (Fig. 13*a*) but sometimes, there was very little after about 20 m of filamentation and sometimes, nothing at all (Fig. 13*b*). However, if the beam diameter is made smaller while keeping the distribution of warm zones roughly the same; i.e., forcing the generated hot spots to be close to one another, we could detect back-scattered fluorescence from the full 100 m propagation length and beyond up to 500 m through extrapolation for all laser shots; also, in the first 10 m, the fluorescence intensity was more than 100 times stronger than the case of larger diameter (25 mm) beam [75]. Theoretical calculation using the same formulation as discussed

Fig. 13. Example of the pulse-to-pulse difference in the back-scattered fluorescence in air as a function of distance. Both (*a*) and (*b*) are under identical laser conditions: 800 nm, 46 mJ, 42 fs.

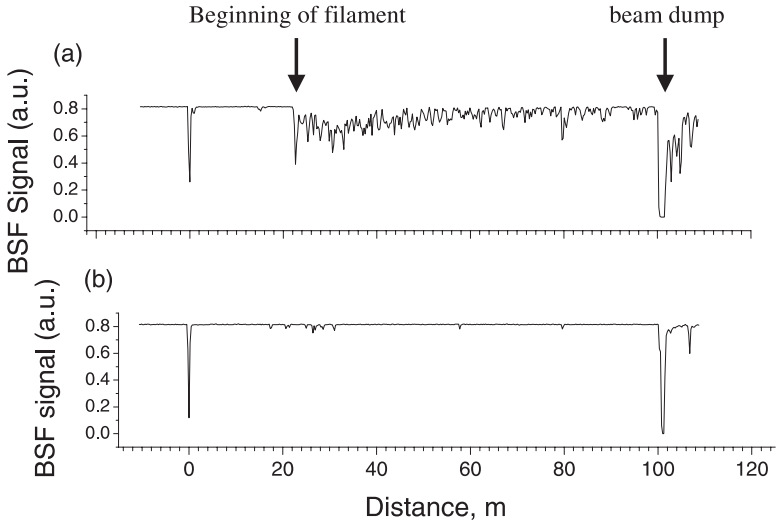

in the case of a single filament but with an input beam pattern consisting of two or more warm zones confirmed these observations [74].

Other groups have calculated what they called either "optical turbulence" effect [76] or "filament fusion and breakup" [78–80] in air through the solution of nonlinear equations similar to (26). Their three-dimensional numerical results were very similar; i.e., there were many high intensity narrow cylindrical zones (multiple filaments) randomly distributed along the propagation direction. Mlejnek et al. [76] interpreted this phenomenon as an optical turbulence effect because they started with a random perturbation across the laser beam pattern and obtained randomly changing filamentation. Tzortzakis et al. [78], Bergé et al. [79, 80] interpreted this as obvious filament fusion and breakup. These interpretations seemed to be based upon the natural "look" of those filament zones that meet or separate randomly. We believe the physics behind all these is the same as what we analyzed above; i.e., filament competition through either field interference effect or energy competition or both.

Another important yet often neglected origin of multiple filamentation in a real experiment is the noncylindrical symmetry of the beam cross section; i.e., a noncircular symmetry of the beam pattern also gives rise to multiple filamentation. A high-power Ti-sapphire femtosecond laser pulse generated by a noncylindrically symmetrical technique using cross beam pumping of the amplifier (a popular method) will certainly give rise to such an effect if spatial filtering is not employed. However, spatial filtering would seldom work at the terawatt level because the pin hole that does the filtering would often be damaged even in vacuum. Under such a situation, the beam pattern is elliptical in shape. The ellipticity depends on the detailed technique of the beam alignment. When such a beam pattern propagates and self-focuses in air, a discontinuous ring, elliptical in shape, would be generated. Several hot zones occur around the elliptical ring. Multiple filamentation could occur from these hot zones if the energy content of the pulse is high enough. The physical reason for creating the hot zones around the elliptical ring is the following.

A slice of such a pulse with elliptical cross section would self-focus towards a line focus where ionization and intensity clamping takes place. This would create, first of all, a line of self-foci (filaments) in practice because the intensity along the line is not uniform. Subsequent divergence of this line source gives rise to an oval-shaped conical wave. Interference with the quasi-plane wave of the background field would result in discontinuous elliptical rings. The discontinuity around the elliptical ring is due

Fig. 14. Patterns of a 45 fs/50 mJ Ti-sapphire laser pulse in air after propagating (*a*) 20 m and (*b*) 80 m. The wavelength of the patterns is around 800 nm, which is the original wavelength of the pulse.

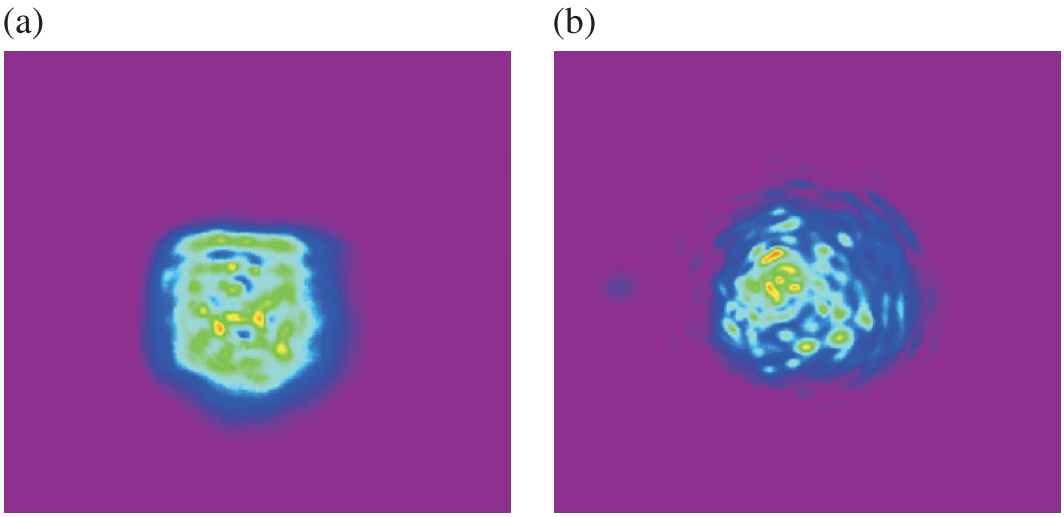

to the fact that the phase difference between the conical field and the quasi-plane wave field changes around the ellipse; hence, there will be constructive and destructive interferences. The pattern of hot zones around the ellipse would be symmetrical though. Such a phenomenon was recently predicted numerically [81]. Such kind of hot zones along a line perpendicular to the propagation axis can also be generated if we use a focusing lens and induce astigmatism. At the focal zone, line focusing due to the astigmatism takes place and the same type of discontinuous elliptical pattern would occur, which would degenerate into multiple filaments [82].

6. Self-guided hot light pulse

In a laboratory experiment, we observed that the diameter of a 45 fs, 1 TW laser pulse's pattern at the original 800 nm wavelength remains practically constant after 100 m of propagation. The white light and the ring structures at the newly generated wavelengths have been filtered away in this experiment. The initial pulse pattern contained a lot of warm zones and the final pattern still contained a lot of hot spots at the end of the propagation path in the corridor of 100 m. Figure 14 shows two patterns, one at 20 m and one at 80 m of propagation. Most of the energy of the pulse is still contained inside the 800 nm part of the pulse. However, when the pulse length was lengthened (positively chirped) to about 200 ps, everything else being identical, the diameter at 100 m was more than three times larger than the initial diameter. The reason for the quasi-maintenance of the beam diameter is due to slice-by-slice self-focusing. Each self-focusing of a warm zone means that the energy of the pulse is sucked towards the self-focal region and then it is released back to the background reservoir after the self-focus. Successive slices would repeat the same process. When there are many self-foci (multiple filamentation), each of the self-foci contributes to sucking energy from the background reservoir towards their respective focal zone and releasing it back to the reservoir. So long as the power in a warm zone is above the critical power for self-focusing, this sucking process would take place and slow down the linear diffraction of the pulse. We call this pulse a self-guided hot light pulse [83]. This is perhaps another indication that the pulse could propagate very far in air and still might give rise to high intensities in the pulse. This optimism is indicated by recent experiments showing that the filaments end at a distance of about 2 km in the atmosphere using 3 TW pulses [16]. A long pulse laser cannot do so.

7. Consequence and applications

To recap, a powerful femtosecond laser pulse propagating in air self-transforms into a chirped white-light laser pulse because of self-focusing, filamentation, self-phase modulation, and self-steepening. The maximum distance over which such a pulse will propagate as a high peak intensity beam could probably be of the order of many kilometres. Measurement of the that distance is a current experimental challenge. The intensity inside a self-focus (filament) is limited by intensity clamping and is of the order of 5×10^{13} W/cm^2. At this intensity, all molecules would be ionized and dissociated with a certain probability. The physics of the interaction of such deformed pulses with molecules is a new subject of research interest.

Because of the possibility of projecting the femtosecond laser pulse at high intensity and long distance in air and because of the self-transformation of the pulse into a white-light laser pulse, it is conceivable to consider the white-light pulse as a lamp in air.[4] This lamp could be used as an active source (as opposed to the "passive" Sun light) to induce absorption of various types of molecules in the atmosphere via back illumination and detection of the absorption on the ground. This is precisely what a team of French and German scientists has done in the past few years by sending up to 5 TW Ti-sapphire laser pulses into the atmosphere and measuring the absorption spectra of the back scattered white-light laser pulse due to various types of pollutant molecules in the atmosphere. The unique laser system, built inside a mobile container through the joint support of the French CNRS and the German DFG (both the organizations are the counter parts of the Canadian Natural Sciences and Engineering Research Council), is nick-named Teramobile, see refs. 11 and 84, and www.teramobile.org). It has been transported to various places including over the ocean to the USA to carry out different types of long-range propagation experiments, including laboratory-scale lightning control [11, 85, 86]. The concept of projecting a white-light laser pulse upward into the atmosphere could also be done in the opposite direction; i.e., sending the laser pulse from a satellite or a space station back into the atmosphere. The resulting self-transformed white-light laser pulse would be much more useful for sensing purposes and other applications since it is now much stronger than the white laser light back-scattered by atmospheric aerosols if the experiment were carried out during the night time. However, this concept would constitute a huge technological challenge.

The high intensity inside the self-foci induces tunnel ionization of molecules that would result in fluorescence. This is the case for nitrogen molecules. This type of fluorescence is practically free from the plasma continuum that is found in breakdown by long laser pulses because of the low plasma density [17, 18, 32]. It is thus natural to apply this observation to ionizing pollutant molecules inside the filament. Measuring the back-scattering fluorescence from the ionization products using a LIDAR system would enable one to detect many pollutant molecules using only one laser source. The challenge is to show that such fluorescence exists and that different molecules have different finger print fluorescence spectra. We have tested several molecules in our laboratory such as fluoro-carbons, hydrocarbons, CO, and CO_2. They all exhibit distinguishable spectra and are always free of plasma continuum. The signal-to-noise ratio in the case of fluoro-carbons is at least similar to that of using LIBS (laser induced breakdown spectroscopy) to detect pollutants samples in the laboratory. We consider this fluorescence technique to be complementary to the white-light back-absorption technique [87].

What is more encouraging with the fluorescence technique is that the fluorescence would be enhanced along the filament directions (backward and forward) because there would be gain of the ASE (amplified spontaneous emission) type. This is proven valid in the nitrogen fluorescence in air [88]. The reason is that in the strong field of the femtosecond laser pulse, molecules would be quickly tunnel-ionized into the continuum state before being dissociated (if any). They then relax back through subsequent molecular states after electron–ion recombination. That is to say, all molecules are first prepared in the

[4] Sauerbrey. Private communication. 1999.

continuum state. When they relax back to the ground state, they have to pass through some fluorescing upper excited states. Before fluorescence takes place, this fluorescing excited state is naturally inverted with respect to lower still empty states. Hence, there is ASE [88].

The high intensity in the self-foci (filament) naturally will induce other nonlinear effects. One of them is third-harmonic generation (THG). It is found that THG in the filament in air is fairly efficient. Theoretical analysis and experiments show that the third harmonic (TH) follows the pump pulse faithfully along the filament and its intensity is also clamped down. We call this new phenomenon self-phase locking [62, 89–91]. Essentially, the nonlinear indices of refraction of both the pump and the TH pulses are influenced by each other's intensity through cross field interaction. The TH intensity being much lower than that of the pump, its influence on the pump is negligible. However, the influence of the pump intensity on the THG is so dominant that the contribution of the TH intensity to its nonlinear index becomes minor. The consequence is that both the TH and the pump have almost equal indices of refraction. Because of intensity clamping, the nonlinear indices are constant; i.e., they have almost equal and constant propagation velocities, hence, self-phase locking. The efficient third-harmonic generation could contribute also to the excitation and ionization of pollutant molecules in air thus reinforcing the detection efficiency.

This new phenomenon and (or) idea of self-phase locking could be extended to any parametric nonlinear process. We could understand this qualitatively in the following way. An nth-order nonlinear parametric process would generate a nonlinear signal wave of frequency ω_n at the self-focal zone of the pump wave whose clamped intensity is much higher than the signal wave. Since the medium is only very weakly ionized (plasma density about 10^{-3} times the medium's atomic density, see discussion later), both waves would interact with each other via the medium's nonlinear polarization generated by the cross fields of the pump and the signal. Such a cross-field-generated nonlinear polarization, which also generates the ω_n wave, would thus be dominated by the pump; hence, the index of refraction or the phase velocity of the signal ω_n wave is dominated by the pump intensity. So long as the pump intensity remains high (which is the case inside the filament), the signal will be "dragged along" by the pump faithfully; i.e., the phase difference is constant and the dispersion of the signal wave would not play a significant role so long as the pump pulse keeps self-focusing into a high (clamped) intensity, which drags the signal wave along with it. Thus, the generation of the signal ω_n wave would be relatively efficient. We should expect efficient generation of not only the third harmonic but the nth harmonic and the nth-order wave due to mixing of n waves in a medium with inversion symmetry (for example, stimulated Raman scattering) whereas in a quadratic $\chi^{(2)}$ medium, all parametric processes such as second harmonic generation, four wave mixing, parametric amplification, etc. would be highly enhanced inside the filament.

The plasma column inside the filament left behind by the series of self-foci gives rise to the emission of electromagnetic [92] and in particular terahertz (THz) pulses [93]. We have measured the effective separation of the electrons and ions along the filament length before they recombine [92]. The recombination gives rise to the radiation of electromagnetic pulses at various frequencies.

If one applies a high voltage between the extremities of this column, a guided discharge is possible. The physics, though, is not what we normally would expect; i.e., it is apparently not the charged column that conducts the electricity. According to the authors, this is probably because the electron density is low and is not uniform along the filament. According to ref. 94 it is due to electron–ion recombination inside the weak plasma column that heats up the central part. The thermal expansion of the heated column leads to a reduction of pressure. The high voltage at the extremities of the plasma column would then discharge through the low-pressure channel. Such discharge mechanisms were first investigated by Vidal et al. [95] where the ideas of density lowering and nonuniformity are clearly expressed. Recent attempts to control lightning in laboratory tests were positive and the future success of this idea seems very promising [86, 96–98].

An experiment by the Teramobile group [11] shows that filamentation inside a cloud chamber can induce nucleation of the supersaturated water vapour. The physics is similar to the standard nuclear physics

experiment in which ion tracks are left behind by gamma rays, for example, and water molecules would nucleate around such ions resulting in water-droplet formation. Ionization inside the filaments would have a similar consequence. We could now stretch our imagination and ask if this observation could apply it to artificial rain making by generating filaments inside a rain cloud containing supersaturated water vapour.

8. Propagation in condensed matter

The physics of self-focusing and filamentation in condensed matter is similar as that in air except that the free-electron generation process is different and that the filament length in all experiments reported to date are much shorter. The free-electron generation process in condensed matter is through the excitation of electrons from the valence to the conduction bands followed by inverse Bremsstrahlung and partial cascade ionization [10, 99, 100]. The pulse duration is too short to allow for a full breakdown. The electron density is estimated to reach 10^{18} cm^{-3}, which is three orders of magnitude lower than the atomic density of condensed matters. All the resulting phenomena, namely, intensity clamping [33], self-phase modulation [33], and conical emission and self-steepening [43] are very similar in condensed matters. One reason why the filament length is shorter in condensed matters compared with air is that the electron density generated in condensed matters is more than two orders of magnitude higher than that in air. Energy loss is thus much larger during propagation; hence, the peak power of the pulse would quickly go below the critical power for self-focusing and filamentation stops. A second reason might be the group velocity dispersion, which is larger in condensed matter than in air. This would increase the pulse duration quickly and hence reduce the peak power during the propagation. A third reason is probably that the critical power for self-focusing is lower ($\sim$ a few megawatts) than that in atmospheric air ($\sim$3–6 GW). Most experiments in condensed matters, including ours, use pulses of relatively lower power, up to several tens of megawatts only, not terawatt pulses.

8.1. Theory of ultrashort pulse propagation in condensed matter

Our theoretical model for nonlinear propagation in condensed matter is based on the wave equation in the slowly evolving wave approximation [66] coupled to the equation for the generation of free-electron density. A similar system of equations was used earlier to describe filamentation in air (see Sect. 4 of this paper). However, in condensed matter one should consider different material equations describing the processes in the nonlinear medium. The change in the material equations is associated with the appearance of avalanche ionization and recombination in addition to tunnel ionization [21] occurring in atmospheric density gases. Assuming the propagation along the z-axis with the group velocity v_g, we will rewrite (26) for the light field complex amplitude $A(x, y, z, t)$ in the form so that all terms that change the spatial or temporal pulse distribution are on the right-hand side of the equation

$$2ik\left(\frac{\partial A}{\partial z}+\frac{1}{v_g}\frac{\partial A}{\partial t}\right)=\left(1-\frac{i}{\omega}\frac{\partial}{\partial\tau}\right)^{-1}\Delta_\perp A-kk''_\omega\frac{\partial^2 A}{\partial t^2}+\frac{2k^2}{n_0}\left[\left(1-\frac{i}{\omega}\frac{\partial}{\partial\tau}\right)\Delta n_{\text{kerr}}+\left(1+\frac{i}{\omega}\frac{\partial}{\partial\tau}\right)\Delta n_p\right]A-ik\alpha A \quad (27)$$

where ω is the laser central frequency, $k=\omega n_0/c$ is the corresponding wave number, and n_0 is the refractive index of the medium.

In (27), the first term on the right-hand side describes diffraction, $\Delta_\perp$ is the transverse Laplacian, the second term describes the group velocity dispersion, where the second-order derivative of the wave number k''_ω is taken at the laser central frequency ω. In the third term, we take into account the nonlinearity of the medium and self-steepening of the pulse in the course of propagation. The last term on the right-hand side of (27) describes the energy losses due to multiphoton electron transitions to the conduction

band. The absorption coefficient $\alpha(I)$ is given by

$$\alpha = I^{-1} m\hbar\omega \left(\frac{\partial N_{\mathrm{e}}^{mpi}(r, z, t)}{\partial t} \right) \tag{28}$$

where m is the minimum number of photons needed for the transition from the valence to the conduction band. The intensity I is expressed through the light field complex amplitude as $I = (1/2Z^2)\,|A|^2$, where $Z = \sqrt{(\varepsilon\varepsilon_0/\mu\mu_0)}$ is the impedance of the medium, ε and μ are dielectric and magnetic constants, respectively. The number of electrons N_{e}^{mpi} is transmitted to the conduction band due to optical-field-induced (multiphoton) transition from the valence band.

The operator $(i/\omega)(\partial/\partial t)$ on the right-hand side of (27) is the result of taking into account the higher order correction terms, in comparison with the slowly varying envelope approximation. These correction terms allow one to describe the propagation of ultrashort pulses with a duration of the order of one optical cycle [66]. In our case, the typical pulse duration generated by the Ti:Sapphire femtosecond laser system is 45 fs (FWHM). This duration corresponds to 16 optical cycles. At the same time the steep fronts formed in the course of propagation require the inclusion of the operator $(i/\omega)(\partial/\partial t)$ into the equation.

The cubic nonlinearity of condensed matter in the case of femtosecond pulse propagation is described by the instantaneous Kerr contribution Δn_{kerr}

$$\Delta n_{\mathrm{kerr}} = \frac{1}{2} n_2 \,|A|^2 \tag{29}$$

The plasma contribution Δn_{p} to the refractive index is given by

$$\Delta n_{\mathrm{p}} = -\frac{1}{2}\left(1 + i\frac{\nu_{\mathrm{c}}}{\omega}\right)\frac{\omega_{\mathrm{p}}^2}{\omega^2 + \nu_{\mathrm{c}}^2} \tag{30}$$

Here $\omega_{\mathrm{p}}^2 = (e^2 N_{\mathrm{e}})/(m_{\mathrm{e}}\varepsilon_0)$ is the plasma frequency, $N_{\mathrm{e}}(r, z, t)$ is the free-electron density, the values m_{e} and e are the electron mass and charge, respectively. By "free" electrons in condensed media we, as suggested in the previous studies [101, 102], mean those electrons whose kinetic energy is large enough that they can move through the liquid or solid lattice without being trapped by localized potential wells; i.e., electrons in the conduction band. In modeling breakdown in condensed matter, transitions between bound and quasi-free states are the equivalent of molecular ionization in gases.

Basically, there are two sources of free electrons when a femtosecond laser pulse propagates and self-focuses through liquids or solids. The first one is direct excitation of the electrons from the valence to the conduction bands by multiphoton absorption [99, 100]. The second is the cascade or avalanche process. In the first case no seed electrons are required since each electron is excited independently. In the second case seed "free" electrons are required to initiate the avalanche. These seed electrons absorb light photons through collision with atoms or molecules in the lattice, a process known as inverse bremsstrahlung absorption [103]. Having acquired an energy greater than the band-gap energy, a "free" electron may excite another electron from the valence to the conduction bands by collision. This produces two free electrons of low energy, which in turn absorb energy from the laser through inverse Bremsstrahlung absorption and excite two more; this process will continue giving rise to an exponential growth of electrons or electron "cascade" leading to breakdown. In an impure medium seed electrons would most likely come from easily excited impurities. In an impure medium with high band gap, multiphoton excitation of several electrons from the impurity states into the conduction band might be enough to initiate the cascade process. Also, in general, there are always some "free" electrons produced from cosmic rays and natural radioactivity [103].

We should note here that optical-field-induced ionization (either multiphoton or tunnel) of atoms or molecules in condensed matter is much less probable when compared with the transition between

the valence and the conduction bands. This is because the band-gap energy is much lower than the ionization potential. One example of this is the following: the band-gap energy in liquid water is 6.5 eV, while the ionization potential of a single water molecule is 12.07 eV. If a laser irradiates at 800 nm, five photons are enough to excite an electron from the valence to the conduction band. At the same time, eight photons are needed to ionize a water molecule. When the laser pulse intensity increases due to either geometrical or self-focusing, the rate of the transitions to the conduction band will be much larger than the ionization rate. The number of electrons in the conduction band will be enough to initiate the avalanche. In comparison with these two sources (quasi-free and cascade electrons), the contribution of electrons coming from molecular ionization will be negligible.

Thus, the equation for the free-electron density growth in condensed media is given by

$$\frac{\partial N_e}{\partial t} = R\left(|A|^2\right)(N_a - N_e) + \nu_i N_e - \beta N_e^2 \tag{31}$$

where the avalanche ionization frequency

$$\nu_i = \frac{1}{W_g}\frac{e^2A^2}{2m_e\left(\omega^2 + \nu_c^2\right)}\nu_c \tag{32}$$

characterizes the inverse time during which the free electron absorbs energy equal to the band-gap energy W_g and hence, produces the next generation of cascade electrons. The elastic collision frequency

$$\nu_c = N_a \nu_e \sigma_c \tag{33}$$

is expressed through the density of N_a, root-mean-square electron velocity v_e, and the electron collision cross section σ_c. The velocity v_e is proportional to the square root of the laser intensity I. Thus, the avalanche ionization frequency (32) depends on the intensity according to $\nu_i \sim I^{3/2}$, if $\nu_c << \omega$.

The optical-field-induced rate R of transitions between the valence and the conduction bands is calculated according to Keldysh theory [57]. The radiative electron recombination coefficient is given by [103]

$$\beta = \frac{8.75 \cdot 10^{-27}}{T^{9/2}} N_e \qquad [\mathrm{cm}^3/\mathrm{s}] \tag{34}$$

where T is the electron temperature in the laser-produced plasma in electronvolts, N_e is measured in cm^{-3}.

In the presence of rapidly developing avalanche ionization, we are immediately faced with the question whether or not there is an optical breakdown in the medium. There are several ways to define the threshold plasma density for optical breakdown. In the study of liquids two possible definitions for the threshold breakdown density were suggested [101, 102]. In water, for example, this density can be defined by the appearance of vapor bubbles in the sample, the "bubble" endpoint, or by the appearance of the visible emission, the "flash" endpoint. The former definition is usually used when studying ultrashort pulses with a duration shorter than 10 ps. In this case, the threshold breakdown density is $N_e^{th} \approx 10^{18}\ \mathrm{cm}^{-3}$. The latter definition is used for a long pulse with a duration of the order of a nanosecond. The threshold breakdown density is then $N_e^{th} \approx 10^{20}\ \mathrm{cm}^{-3}$. Another possible definition of the breakdown threshold density is the critical density of the plasma $N_{cr} = \omega^2 m_e \varepsilon_0 / e^2$, where m_e and e are electron mass and charge, respectively, ω is the central laser frequency. This definition was used, for example, for studying the breakdown in fused silica in ref. 104. In the experiments performed at Laval University, a beam with the following conditions: 45 fs, 810 nm pulses with 0.2–3 μJ energy, and a beam diameter of 5 mm was focused into the water cell with different microscope objectives [105]. The most appropriate definition of the threshold breakdown density is $N_e^{th} \approx 10^{18}\ \mathrm{cm}^{-3}$, since in the experiment the breakdown was detected by the scattered IR light of the laser and not by the visible

emission. Knowing the threshold density N_e^{th}, one can estimate the breakdown threshold intensity I_{th} in water. To estimate, let us consider only the avalanche term in (31), i.e., we start from the equation

$$\frac{\partial N_e}{\partial t} = \nu_i N_e \tag{35}$$

the solution to which is

$$N_e(t) = N_{e0} \exp(t\nu_i) \tag{36a}$$

where N_{e0} is the background or seed electron density in the medium. The ionization frequency ν_i needed to cause the avalanche can be expressed as (from (36a))

$$\nu_i = \frac{\ln\left(N_e^{th}/N_{e0}\right)}{t} \tag{36b}$$

Let us take the threshold breakdown density as $N_e^{th} \approx 10^{18}$ cm^{-3}, corresponding to the "bubble endpoint", and the background electron density in water $N_{e0} \approx 10^{10}$ cm^{-3} as suggested in ref. 106. The ratio $N_e^{th}/N_{e0} = 10^8$ and the corresponding avalanche ionization frequency is then $\nu_i \approx 18/t$ (from (36a)). For the time scale of the order of $t = 45$ fs, which was full-width-half-maximum pulse duration in the experiment, the frequency ν_i should be 4×10^{14} s^{-1} to cause the avalanche. Substituting (33) for the elastic collision frequency ν_i into the (32) for the avalanche ionization frequency, we obtain the dependence of the intensity on the frequency ν_i. Considering the laser central wavelength as 810 nm, the medium parameter for water as $W_g = 6.5$ eV, the density of the neutral water $N_a = 3.3 \times 10^{22}$ cm^{-3} and the cross section $\sigma_c = 10^{-15}$ cm^2 [103], we obtain the threshold breakdown intensity $I_{th} = 1.4 \times 10^{13}$ W/cm^2 (from (32, 33)). We note that the value I_{th} is not very sensitive to the ratio N_e^{th}/N_{e0}. The increase of the threshold density N_e^{th} from 10^{18} cm^{-3} to the critical plasma density 10^{21} cm^{-3} leads to the change in the intensity I_{th} from 1.4×10^{13} to 1.8×10^{13} W/cm^2, respectively. Earlier experiments and calculations of the breakdown threshold intensity give us $I_{th} = 5.4 \sim 5.6 \times 10^{12}$ W/cm^2 for a 100 fs pulse [101, 102] and the breakdown intensity in the experiment performed in Laval university was 1.2×10^{13} W/cm^2 [105].

Optical breakdown may prevent the formation of light filaments in condensed matter. This might happen if the threshold intensity needed for the breakdown is reached earlier in the propagation than the self-focusing starts to noticeably affect the pulse transformation. Even if the peak power of the pulse is below the critical power for self-focusing, optical breakdown can occur on the condition of tight geometrical focusing. Another limiting case is a pulse without external focusing, but with the peak power higher than the critical power for self-focusing. In this latter case the filament or multiple filaments will be formed without breakdown. The reason for this is that self-focusing induces a strongly convergent wave front only in a narrow transverse region, which contains the peak power of the order of the critical power for self-focusing in the material [28]. A small number of electrons produced by the multiphoton ionization will be enough to limit intensity increase and prevent further ionization. In all the intermediate cases, the presence or absence of the optical breakdown will be defined by a specific combination of the geometrical focusing distance and the ratio of the pulse peak power to the critical power for self-focusing in the medium.

The detailed theoretical and experimental studies of optical breakdown and filament formation in water under different focusing conditions are studied in ref. 105. In continuation of this research, we present here the plots with partial contribution of the avalanche and multiphoton electrons to the total quasi-free electron density in the vicinity of the geometrical focus. The ratio of the on-axis peak electron density, N_e, to the neutral density of the neutral water molecules, N_0, as a function of propagation distance is shown in Fig. 15 for three geometrical focusing distances $f = 16.9$ mm ($f/d = 3.4$, where d is the beam diameter on the lens), 43.1 mm ($f/d = 8.6$), and 73.5 mm ($f/d = 14.7$)

Fig. 15. The simulated on-axis distribution of multiphoton and avalanche electrons with propagation distance z in the water cell. In the simulations the input pulse energy was 0.4 mJ, pulse duration 45 fs, input beam diameter 5 mm, geometrical focusing distance (*a*) $f = 16.9$ mm, (*b*) $f = 43.1$ mm, and (*c*) $f = 73.5$ mm.

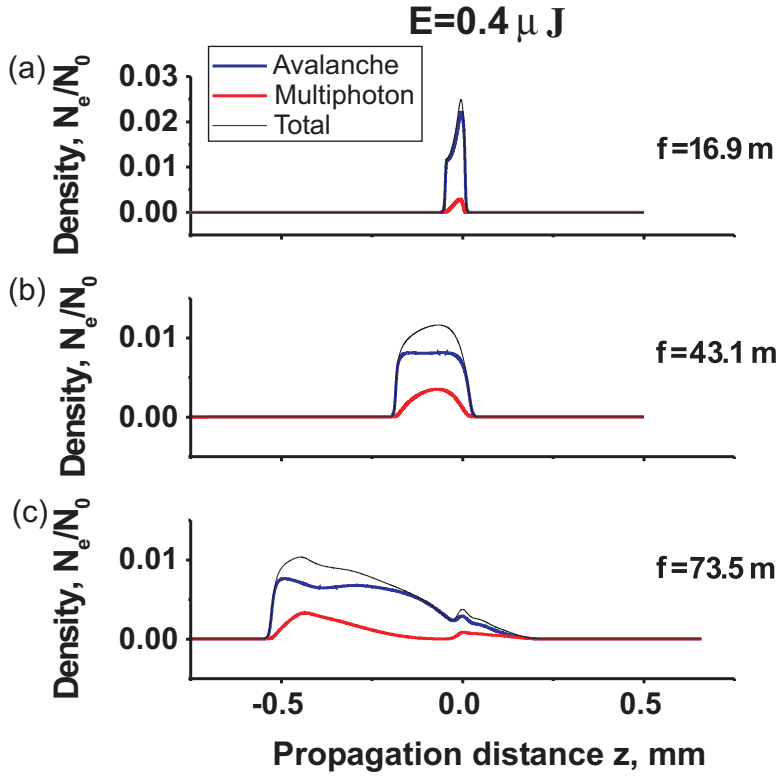

Fig. 16. Experimental visualization of multiple re-focusing through three-photon fluorescence in methanol. (*a*) Experimental set up to photograph the fluorescence from the side and (*b*) picture of multiple refocusing.

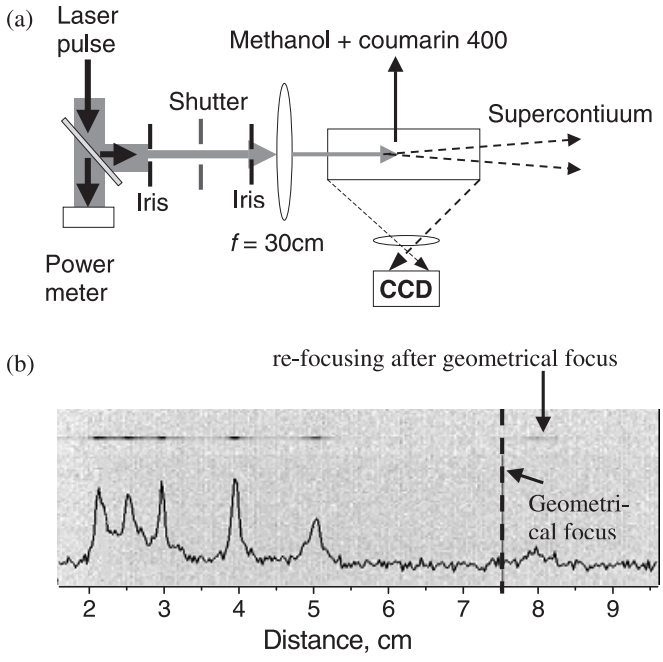

and input pulse energy 0.4 μJ. The blue line corresponds to the partial contribution of avalanche electrons, the red line corresponds to partial contribution of multiphoton electrons, and the black line is the total plasma density. The focal position corresponds to $z = 0$. In the case of tight focusing ($f = 16.9$ mm, Fig. 15*a*) the plasma in the focal volume is provided mainly by the avalanche. The latter is in agreement with the experimental data: optical breakdown at the focal volume is registered for these input pulse energy (0.4 μJ) and focal distance ($f = 16.9$ mm). Increase in the focal distance up to $f = 43.1$ mm while preserving the same input pulse energy leads to an increase of the partial contribution of multiphoton electrons and elongation of the focal volume towards the lens (Fig. 15*b*). In accordance with the experimental data, for this energy, we are just slightly above the breakdown threshold for this intermediate focal length of $f = 43.1$ mm. The slight extension of the plasma towards the focusing lens due to plasma absorption is well known in long-pulse optical breakdown (see, for example, ref. 107. The case of filamentation where the geometrically focused intensity (linear propagation) is below the optical breakdown threshold is shown in Fig. 15*c*. The total plasma length is 0.7 mm, that is ten times larger than that in Fig. 15*a* and three times larger than that in Fig. 15*b*. However, the total electron density is lowest in Fig. 15*c*. According to the experiment, in the case of $f = 73.5$ mm, a pulse with an input energy of 0.4 μJ propagated in the filamentation regime does not cause optical breakdown in water. Thus, partial contribution to avalanche and multiphoton electrons as well as to the total number of electrons in the conduction band is very sensitive to the focusing geometry of the experimental set-up. After a femtosecond pulse has gone, the electrons recombine and deposit their energy into the condensed matter (see Sect. 10 for the consequence). In conclusion of this section, we note that quasi free electrons, created in condensed matter through the avalanche process, should not be ultimately associated with the onset of breakdown. Instead, the so-called avalanche electrons may just partially contribute to the total number of quasi-free electrons in the medium and together with "multiphoton" electrons change the refractive index.

9. Visualization of filamentation in liquids

It is instructive to visualize experimentally the evolution of filamentation. Figure 2 is one example of refocusing in air. It is even more spectacular in a dilute dye solution in which two- or three-photon fluorescence reveals the filamentation path clearly. Liu et al. [108] has observed up to six refocusing filaments revealed by three-photon fluorescence in a dilute solution of coumarin in methanol. Figure 16 shows the experimental set-up and the resulting multiple refocusing.

Schroeder and Chin [109] showed the full evolution of filaments from the start of self-focusing through group velocity dispersion, intensity clamping, self-phase modulation, and ending at self-steepening. The experiment was done by shining a Ti-sapphire laser beam (1 kHz, 810 nm,1.9 mJ, $T_{1/e} = 46$ fs, and $r_{1/e} = 4.3$ mm where $T_{1/e}$ and $r_{1/e}$ are the duration and radius of the pulse at the $1/e$ level, respectively,) through a slit set next to the window of a dye cell containing Rhodamine B in methanol at a concentration of 3×10^{15} cm^3. Figure 17 shows the resulting set of filaments visible to the eyes. These pictures were taken from the side of the dye cell showing propagation and filamentation from left to right. Figure 18 singles out one of the so-called mature filaments [109]. This mature filament goes through the following physical processes: self-focusing, group velocity dispersion, intensity clamping, self-steepening, anti-Stokes spectral broadening, and multiple-filaments competition. We give a description in what follows.

The top panel in Fig. 18 is the image of this filament. The main panel shows a z-scan of the fluorescence intensity through the center of the filament ($\Delta y \sim 15$ μ m) and the corresponding diameters (FWHM). A number of stages are observed and are marked by arrows.

Region 1 Group velocity dispersion

The slit-clipped laser beam enters the Rhodamine B/methanol solution at $z = 0$. This region is somewhat masked by the body of the sample cell. The filament becomes discernible at about $z = 1.9$ mm.

Fig. 17. Visualization of the full set of multiple filamentation in rhodamine B dissolved in methanol. These pictures were taken from the side of the dye cell. The vertical dimension is the length of the slit while the horizontal dimension is along the propagation direction showing the evolution and the length of the filaments. The slit is set at the left-hand edge of the picture.

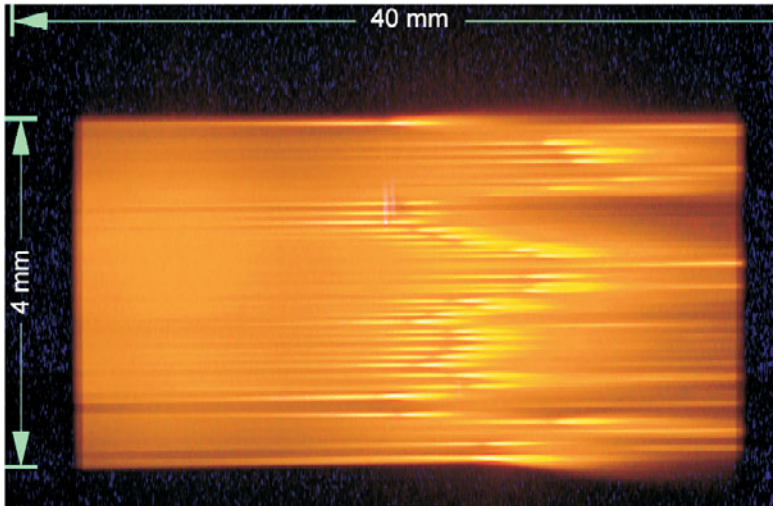

The diameter is about 65 μm and decreasing. The "plateau" of fluorescence between $z = 0$ and 3.4 mm corresponds to the zone in which self-focusing is influenced by the group velocity dispersion, which has a tendency to lengthen the pulse thus lowering the intensity. At the beginning between $z = 0$–1.9 mm, the fluorescence intensity is almost constant, indicating that the effect of group velocity dispersion (pulse lengthening) roughly compensates that of self-focusing resulting in a constant laser intensity in the filament. After $z = 1.9$ mm, the fluorescence decreases slightly. The slight decrease in fluorescence indicates that the rate of decrease of the laser intensity (via pulse lengthening by dispersion) is slightly larger than the rate of increase of the laser intensity by self-focusing. Starting at $z = 3.4$ mm, the fluorescence intensity increases significantly.

Region 2 Self-focusing collapse

From $z = 3.4$ to 7.2 mm, the fluorescence signal rises while the diameter of the filament keeps shrinking. This would indicate that self-focusing effect overcomes dispersion leading to a quick increase of the peak intensity of the pulse. The increase of intensity induces an increase in the two-photon absorption by the dye molecules. Hence, the subsequent fluorescence increases.

Region 3 Intensity clamping

At around the position 7.2 mm where the fluorescence intensity reaches a first maximum, the peak of the pulse reaches its balancing point. At this point the generated electron density in the conduction band defocuses the central most powerful slice of the pulse [9, 26]. This is where the intensity is clamped [20, 32, 33]. Because this is where the most powerful slice self-focuses, more energy is deposited and the intensity of the subsequent two-photon fluorescence is highest. This most powerful slice would then diverge and would not contribute much to the two-photon fluorescence. Other slices of the pulse undergo intensity clamping at later positions downstream. The two-photon fluorescence would be less intense because the energy content of these slices is decreasing as compared to that of the most powerful slice. In other words, while the peak intensity is clamped, the diameter of these intensity clamping zones decreases. The latter is indicated in Fig. 18 between 7.2 and 8.4 mm. At 8.4 mm, there is a minimum in the fluorescence intensity. But this minimum position is not yet the end of the filament.

Fig. 18. Evolution of a mature single filament.

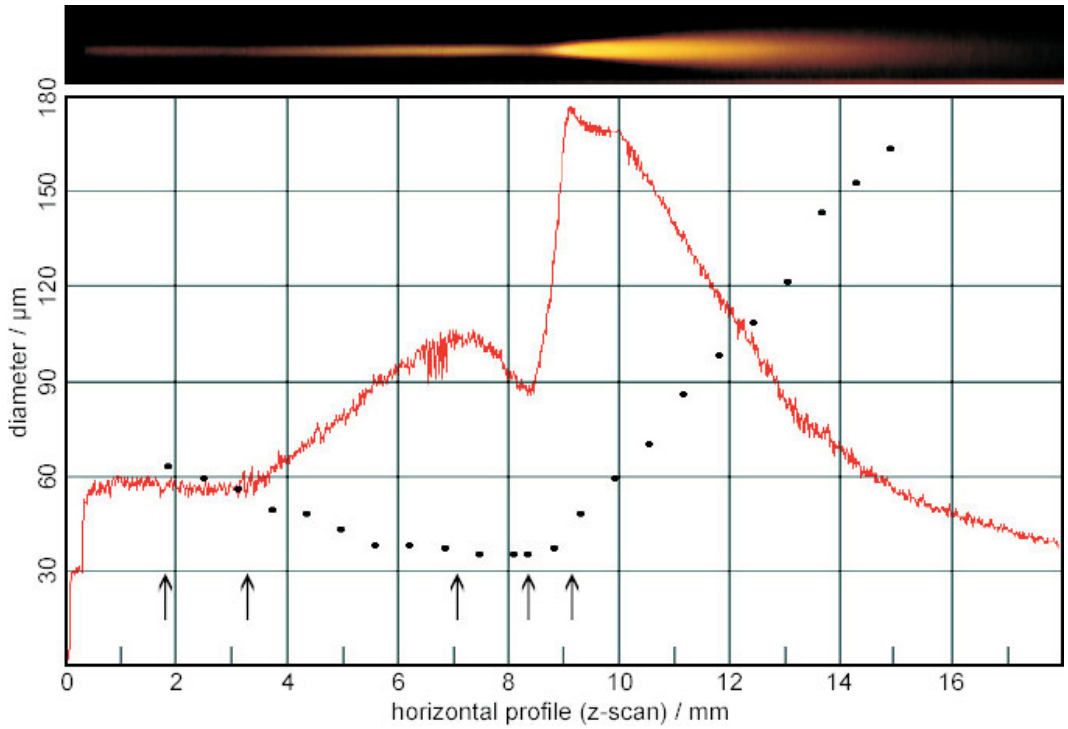

Region 4: Self-steepening

The fluorescence intensity suddenly rises quickly after the minimum. We attribute this rise to the fluorescence induced by single-photon absorption. This can be attributed to the supercontinuum generation or white-light laser [9, 10]. The latter has a huge broadening towards the blue side of the laser's original spectrum from 810 nm to about 350 nm [33]. The dye molecules are excited by one-photon absorption of the continuum light ($\sigma^{(1)}_{550\ \mathrm{nm}} = 4 \times 10^{-16}\ \mathrm{cm}^2$), which is much more efficient than the two-photon excitation process at the available intensity; hence, there is an abrupt increase in the fluorescence intensity.

In a focusing geometry, the increase of the fluorescence intensity followed by a minimum could also be explained by two-photon absorption saturation of the dye molecules in the focusing volume [110, 111]. If this were so, there should be two maxima of similar widths and heights around the minimum. However, in Fig. 18 the fluorescence intensity suddenly increases strongly after the minimum. This sudden increase cannot be explained by the consequence of saturation.

It is well known that the filament would end around the position of the diffraction length [26]. Before reaching the end of the filament, the pulse would quickly undergo self-steepening [43, 44]. This would quickly broaden the spectrum of the pulse towards the shorter wavelength side making the pulse white. According to refs. 43 and 44, pure self-phase modulation in the self-induced plasma is not as broad as that due to self-steepening. Thus, during the intensity clamping process and before self-steepening, no single photon fluorescence would occur. The steep rise in the fluorescence intensity would correspond to the zone of self-steepening that generates strong frequency components below 600 nm and to about 350 nm [10, 33, 99, 100]. The final decay of the one-photon fluorescence is caused by the absorption of the white-light beam. In fact, this decay is faster at higher dye concentrations.

The sharp rising part of the fluorescence intensity curve corresponds to where white light is generated due to self-steepening. It spans a distance of roughly 0.8 mm. This is in agreement with the filament

length measured in a previous publication [50]. There, the filament length was measured in water and other liquids and found to be of the order of 1 mm. The definition of the filament length in that work was the length of the zone at which white light was generated.

After self-steepening, the filament would end; i.e., the hot spot would diverge out. We define this as a mature filament. If there is still enough energy after self-steepening, the pulse will refocus again and this is what is known as the refocusing phenomenon [26, 108].

10. Melting of glass and wave-guide writing in glass

During self-focusing of powerful femtosecond laser pulses in bulk glass (fused silica or quartz), the free electrons generated in the conduction band will return back to the valence band through radiative and nonradiative transitions and through the formation of excitons followed by self-trapping [112]. The relaxation of a self-trapped excitons leads to the formation of an intrinsic structural defect. If the transition were radiative, it would generate UV photons whose energy would be as large, or larger, than the band-gap energy. Such photons would be re-absorbed by the electrons in the valence band and would finally turn into heating the local zone. Thus, both radiative and nonradiative transitions would lead to a local heating of the glass material. We have observed that such heating leads to the melting of glass [113–115]. The ejected powder from glass surfaces shows beads of smooth and round (signs of melting) micrometre- and sub-micrometre-sized particles observed under a scanning electron microscope. X-ray diffraction shows that using 1 kHz repetition rate 180 fs Ti-sapphire laser pulses to generate the powder, fused silica partially crystallizes into several types of high-pressure SiO_2 crystals. However, only melting but no crystallization was observed in the case of quartz [115]. (Note that crystallization in fused silica is also another sign of melting because crystals can only be formed from a hot liquid phase.) We attribute this to the higher thermal conductivity in quartz, which dissipates the heat between pulses quickly so that there is no generation of high pressured. The details of the physics of this type of modification of the thermodynamic state of materials using femtosecond laser pulses is being studied in our laboratory.

In 1996, Hirao's group [116] discovered that femtosecond laser pulses can write wave guides in fused silica. Since then, many groups have studied different ways of writing wave guides and the reason why there is a change in the index of refraction is still a subject of debate. Our study indicates that melting and filamentation are responsible for the writing of a good wave guide. Under certain focusing conditions, filamentation dominates the propagation. The local "gentle" melted material inside the filament zone would cool down resulting in a uniform higher index of refraction. This would give rise to a good wave guide when the laser pulse is scanned through a linear zone [117]. Much stronger focusing conditions would merge the self-focus and the geometrical focus together and the ionization in this mixed zone would be stronger though still not strong enough to give a total breakdown. Nevertheless, a small local explosion would occur that would result in voids. Such voids would not favor the formation of good wave guides [118].

11. Summary

A powerful femtosecond laser pulse propagating in an optical medium self-focuses to a rather high but limited intensity that we call intensity clamping. It is about 5×10^{13} W/cm^2 in air. It self-transforms into a chirped white-light laser pulse. The broad spectrum is popularly called a supercontinuum. In air, the spectrum extends from the near UV ($\sim$350 nm) to the infrared ($\sim$4 μm). The spectral width depends on the ionization potential (gases) or the band gap energy (condensed matter). An efficient third harmonic pulse at around 267 nm is generated inside the filament and it follows the fundamental self-focusing pulse "faithfully". This is a new phenomenon called self-phase locking. The recombination decay of the plasma column generates a weak but measurable electro-magnetic signal in the terahertz regime. Some potential applications include making use of the back-scattered white light as a source to

measure pollutant absorption using the LIDAR technique. This was, and still is, being exploited by the French and German consortium using the unique Teramobile. It is also conceivable to use the LIDAR technique to measure the back-scattered fluorescence from the ionized and fragmented molecules inside the filaments in the path of propagation. This latter technique together with the possibility of ASE type of gain in the signal is being studied in the Chin's laboratory. One could take advantage of the resulting plasma "channel" left behind by filamentation and apply it to lightning control and probably even artificial rain making. In glass, filamentation leads to local melting, which results in a change in the index of refraction and is the origin of wave-guide writing. The resolidification of the melted glass could transform the thermodynamic state of glass into various forms of SiO_2 crystals.

12. Challenges ahead

We have come a long way in the understanding the physics of self-focusing and filamentation of powerful femtosecond laser pulses. Through this understanding, many new questions on fundamental nonlinear physics arise. Furthermore, this filamentation phenomenon gives rise to a lot of possibilities for potential applications through the use of the results of such nonlinear propagation, which is not found in the linear propagation of a "normal" laser beam: the self-transformed very broad band white-light laser pulse, the strong intensity inside the filament, the efficient generation of third and higher harmonics, the electromagnetic pulse generated along the filament, the ASE type of gain in the fluorescence of molecules excited inside the filaments, etc. Many applications have just begun and it is difficult, at this point, to see the limit of the technique. The following attempts to give a closer look at what lies ahead of us. The number of subjects are only partial.

12.1. The physics of filamentation

From a physics point of view, there are still some details of the propagation that need to be understood or clarified. Examples are the following.

(*a*) **Filament with or without plasma generation:** So far in this paper, the definition of a filament is the plasma column left behind by the series of self-foci. However, recently, there are papers that claim that filaments could be formed without plasma generation. Kasparian et al. [119] used a ray-tracing technique to describe self-focusing in the stationary case. They considered the mutual influence of the subrays of the beam due to the Kerr nonlinear index change created by each ray. They concluded that ray tracing with a purely Kerr self-focusing effect can lead to filamentation without ionization. This ray-tracing technique is good in the stationary approximation to determine the self-focal position. However, it can hardly explain the complicated features in real experiments where plasma formation and multiple filamentation are observed. Moreover, in the real case of a femtosecond pulse, a ray would see the instantaneous nonlinear index change due to another ray only when they have spatial overlap within a distance of 30 μm for a 100 fs pulse (speed of light $\times$ 100 fs). Such overlap would be difficult in the off-axis region and cannot be treated using stationary approximation. Dubietis et al. [120] used a CW model and calculated only the fluence of the pulse propagating in water. The paper uses nonlinear absorption saturation as a stabilizing mechanism. Its effect is similar to ionization. Calculating only the fluence and neglecting supercontinuum, it is very hard to distinguish nonlinear absorption from the nonlinear ionization. To clarify this point, it is necessary to both show time-resolved pictures and carry out experiments to precisely measure the electron density inside the filament. This leads to the following comment.

(*b*) **Electron density inside a filament:** The electron density inside a filament has been measured in air but the value varies over a few orders of magnitude (from $\sim 10^{14}$ to $\sim 10^{18}$ cm^{-3}) [13, 17, 29–31, 45, 121]. In condensed matters, the authors of refs. 122 and 123 measured the electron density in glass and give a maximum value of $\sim 5 \times 10^{19}$ to 6×10^{19} cm^{-3}. Precision measurement

of the electron density would clarify many of the physical concepts of the filamentation process. In particular, because of intensity clamping, the transverse size (diameter) of a filament would be larger with higher input energy of the pulse (assuming single filamentation and before multiple filamentation sets in). When the energy of the pulse is reduced to near but above self-focusing threshold, the diameter of the filament where there is intensity clamping (hence plasma generation) would be so small that it might defy even the most precise measurement. This might be the situation where experimentalists claimed to have observed filaments without ionization [124]. Only the capability of a precise measurement of the electron density inside a small diameter would answer this challenging question.

(*c*) **The ultimate length of a filament:** The ultimate length of a filament in air, be it single or multiple, is an important quantity of interest to all those who have remote sensing in mind. This experiment is not trivial; it is hampered by the detection sensitivity at long distance and the capability of bringing the laser to a suitably long detection range for controlled measurement. The sensitivity of nonlinear propagation to wave-front imperfection and distortion as well as the complication of filament competition are factors that would limit the filament length. Beam quality is thus an ultimate issue in such kind of long-distance propagation and sensing. So the effect of turbulence on the propagation of short intense pulses must be studied since it strongly affects the wave front. The Teramobile is a partial answer but so far this is the only system known to the open scientific community. More such systems should be built to enhance research in this field but, the system being expensive, it would probably take a major effort and international collaboration to make this happen in the short run.

(*d*) **The death of a filament:** The length of the filament is intimately related to the question of how a filament dies. We have justified that soon after self-steepening, that particular filament ends but it could be followed by re-focusing. The question is how and why does the filament stop? Is it due to local diffraction or is it due to energy dissipation? After one filament dies away, how does re-focusing start again? A quantitative model to explain the physics of how a filament dies is still lacking.

(*e*) **Control of multiple filamentation:** Because all practical laser pulse fronts are not perfect, multiple filamentation at high pulse energy is unavoidable. Also, turbulence in the air would also lead to a random change of the wave front for long-distance propagation. The question is how one could control multiple filamentation [125]. This challenge would have many practical consequences. For example, one would like to overcome and (or) make use of multiple filamentation and still able to generate strong filamentation at long distances into the atmosphere.

(*f*) **Soliton:** There is this question of whether filamentation could be described by the propagation of a soliton even though there is constant loss of energy of the pulse.

(*g*) **Few-cycle pulse:** In the theory of propagation described in Sect. 4, we explained that the full Maxwell equations will have to be solved during the propagation of a few cycle pulses. The visual model and (or) picture of slice-by-slice self-focusing would also breakdown since the concept of a slice is essentially a cut of the intensity envelope of the pulse. That is to say, the temporal thickness of a slice has to be at least one cycle of the field oscillation because the definition of intensity is the cycle average of E^2 where E is the instantaneous electric field. This definition is good if during one cycle, the field does not change significantly. With a few-cycle pulse, the field amplitude changes significantly from one half-cycle to another. The cycle average would not make much sense any more. The physical concept would have to be changed to that of purely field interaction.

Fig. 19. Ultra-broad band generation after filamentation in air using 5 mJ/45 fs Ti-sapphire laser pulses. The laser was focused by a 3.75 m focal length lens. At such a high pump energy, the third harmonic undergoes cross-phase modulation with the pump and is so much broadened that it merges with the normal supercontinuum of the pulse that ends normally at 350 nm. The evolution of such a change as a function of pump energy is given in ref. 91.

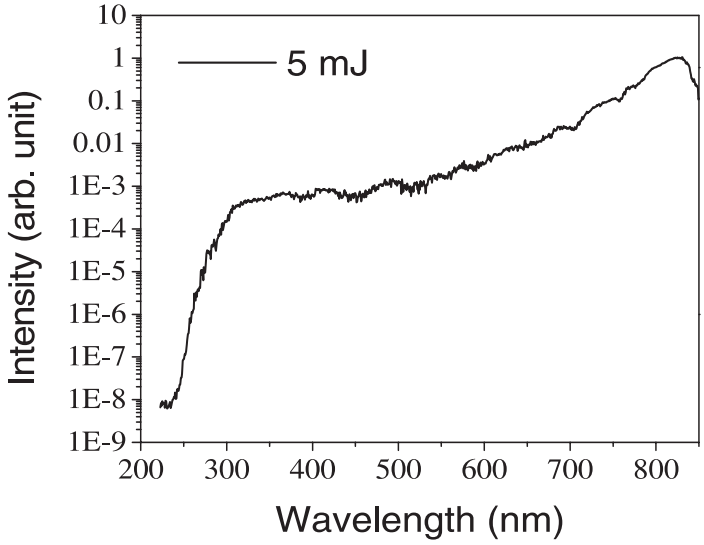

(*h*) **Self-phase locking:** The general physics of self-phase locking [62, 89] in all parametric processes needs to be explored further in a more quantitative way.

(*i*) **Cross-phase-modulation between third harmonic and the pump:** The generation of a super-broad continuum spanning from a few micrometres in the IR to about 220 nm in the UV after filamentation in air was recently demonstrated. Figure 19 shows such a broad spectrum [91]. This spectrum shows the merging of two broad spectra at high pump energy (5 mJ/45 fs): the normal supercontinuum that ends around 350 nm and the broadened third harmonic spectrum due to cross-phase modulation with the pump. It results in such a super-broad spectrum. A similar result was obtained by the Teramobile group [126]. Using 10 fs Ti-sapphire laser pulses, Trushin et al. [127] observed a similar broad spectrum in argon but using much less than 0.3 mJ per pulse. The qualitative physics is explained it in terms of cross-phase modulation between the pump and the third harmonic generating a broad UV spectrum that fills up the gap between the supercontinuum of the pump and the third harmonic [62, 89]. The detailed physics, in particular, that of the much more efficient generation of the continuum using 10 fs or shorter pulses, should be explored.

12.2. Applications of filamentation

(*a*) Remote sensing in the atmosphere lacks long-distance laboratory tests; this drawback was mentioned in the last paragraph.

(*b*) Lightning control [86, 96–98] needs to have more physical studies. It is not clear if the main effect is really the direct electrical conduction by the plasma channel of the filament since the plasma is of such a low density ($\sim 10^{16}$ cm^{-3}). The other model, [94] and [95], of thermal expansion in the plasma column resulting in a low-pressure zone in a short filament inside the laboratory seems to be reasonable as discussed above. Yet no further confirmation of this latter model was made in longer range induced discharge studies done by the same group together with other authors [96].

(*c*) Condensed matter: A quantitative model is needed to describe the melting of glass [115] for the sake of writing wave guide and data storage, etc.

(*d*) Ionization and dissociation: The consequence of the deformation of the femtosecond laser pulse passing through optical media (windows for example) before arriving at the focal zone has started to show up in recent experiments of ionization and dissociation of molecules [128, 129]. Toluene molecules showed more efficient fragmentation because of the pulse deformation. The self-focusing effect through the optical media shifted the focal volume. This experiment can easily explain why many of the results in recent years in the fragmentation of complex molecules are not coherent (see refs. 128 and 129 for more detail) because none of them was aware of this important effect; i.e., the femtosecond laser peak power and the material distance through which the laser pulse passed before arriving at the focal zone where interaction took place were different from experimental set-up to experimental set-up.

(*e*) Pulse compression and few cycle physics: what we have known since the very beginning of numerical calculation of the pulse deformation, shortening, and splitting during propagation is now being applied to the very important field of pulse compression generating few cycle or even down to one cycle pulses with high energy [12, 127, 130, 131]. This compression technique, which can generate few cycle pulses at high energy is very simple and efficient. It would open up the door for more studies of few cycle laser interaction physics including the generation of attosecond laser pulses. The propagation of such pulses constitutes also a new challenge as mentioned above in Sect. 12.1*d*.

Acknowledgement

This paper represents the fruit of many years of research supported by Natural Sciences and Engineering Research Council, Canada Research Chairs, Canada Foundation for Innovation, Defence Research and Development Canada-Valcartier, Critical Infrastructure Protection Initiative, Le Fonds Québécois de la Recherche sur la Nature et les Technologies, Femtotech of Valorisation Recherche Québéc, the Alexander von Humboldt Foundation (Germany), and NATO. SLC, VPK and OGK acknowledge the partial support of NATO-linkage grants. VPK and OGK were partially support by the Russian Foundation of Fundamental Research and the European Research Office of the US Army. NA acknowledges the support of the US Army Research Office and AMCOM.

References

1. M. Hercher. JOSA **54**, 563 (1964).
2. R.Y. Chiao, E. Garmire, and C.H. Townes. Phys. Rev. Lett. **13**, 479 (1964).
3. J. Reintjes, R.L. Carman, and F. Shimizu. Phys. Rev. A, **8**, 1486 (1973).
4. E. Yablonovitch and N. Bloembergen. Phys. Rev. Lett. **29**, 907 (1972).
5. C.G. Morgan. Rep. Prog. Phys. **38**, 621 (1975).
6. A. Braun, G. Korn, X. Liu, D. Du, J. Squier, and G. Mourou. Opt. Lett. **20**, 73 (1995).
7. L. Wöste, C. Wedekind, H. Wille et al. Laser . Optoelektron. **29**, 51 (1997).
8. R.R. Alfano (*Editor*). The supercontinuum laser source. Springer Verlag, Berlin. 1989.
9. S.L. Chin, A. Brodeur, S. Petit, O.G. Kosareva, and V.P. Kandidov. J. Nonlinear Opt. Phys. Mater. **8**, 121 (1999).
10. V.P. Kandidov, O.G. Kosareva, I.S. Golubtsov, W. Liu, A. Becker, N. Aközbek, C.M. Bowden, and S.L. Chin. Appl. Phys. B, **77**, 149 (2003).
11. J. Kasparian, M. Rodriguez, G. Méjean et al. Science, **301**, 61 (2003).
12. C.P. Hauri, W. Kornelis, F.W., Helbing, A. Heinrich, A. Couairon, A. Mysyrowicz, J. Biegert, and U. Keller. Appl. Phys. B, **79**, 673 (2004).
13. B. La Fontaine, F. Vidal, Z. Jiang et al. Phys. Plasmas, **6**, 1615 (1999).

14. S.A. Hosseini, Q. Luo, B. Ferland, W. Liu, N. Aközbek, G. Roy, and S.L. Chin. Appl. Phys. B, **77**, 697 (2003).
15. G. Méchain, C. D'Amico, Y.-B. André et al. Opt. Commun. **247**, 171 (2005).
16. M. Rodriguez, R. Bourayou, G. Méjean et al. Phys. Rev. E, **69**, 036607 (2004).
17. A. Talebpour, M. Abdel-Fattah, and S.L. Chin. Opt. Commun. **183**, 479 (2000).
18. A. Talebpour, M. Abdel-Fattah, A.D. Bandrauk, and S.L. Chin. Laser Phys. **11**, 68 (2001).
19. A. Becker, A.D. Bandrauk, and S.L. Chin. Chem. Phys. Lett. **343**, 345 (2001).
20. J. Kasparian, R. Sauerbrey, and S.L. Chin. Appl. Phys. B, **71**, 877 (2000).
21. S.L. Chin. *In* Advances in multiphoton processes and spectroscopy. Vol. 16. *Edited by* S.H. Lin, A.A. Villaeys, and Y. Fujimura. World Scientific, Singapore. 2004. pp. 249–271.
22. M. Mlejnek, E.M. Wright, and J.V. Moloney. Opt. Lett. **23**, 382 (1998).
23. M. Mlejnek, E.M. Wright, and J.V. Moloney. IEEE J. Quantum Electron. **35**, 1771 (1999).
24. V.P. Kandidov, O.G. Kosareva, and A.A. Koltuna. Quantum Electron. **33**, 69 (2003).
25. E.T.J. Nibbering, P.F. Curley, G. Grillon, B.S. Prade, M.A. Franco, F. Salin, and A. Mysyrowicz. Opt. Lett. **21**, 62 (1996).
26. A. Brodeur, C.Y. Chien, F.A. Ilkov, S.L. Chin, O.G. Kosareva, and V.P. Kandidov. Opt. Lett. **22**, 304 (1997).
27. R.W. Boyd. Nonlinear Optics. 2nd ed. Academic Press, Boston. 2003.
28. J.H. Marburger. Prog. Quantum Electron. **4**, 35 (1975).
29. H. Schillinger and R. Sauerbrey. Appl. Phys. B, **68**, 753 (1999).
30. S. Tzortzakis, B. Prade, M. Franco, and A. Mysyrowicz. Opt. Commun. **181**, 123 (2000).
31. C.Y. Chien, B. La Fontaine, A. Desparois, Z. Jiang, T.W. Johnston, J.-C. Kieffer, H. Pepin, F. Vidal, and H.P. Mercure. Opt. Lett. **25**, 578 (2000).
32. A. Becker, N. Aközbek, K. Vijayalakshmi, E. Oral, C.M. Bowden, and S.L. Chin. Appl. Phys. B, **73**, 287 (2001).
33. W. Liu, S. Petit, A. Becker, N. Aközbek, C.M. Bowden, and S.L. Chin. Opt. Commun. **202**, 189 (2002).
34. M. Fujimoto, S. Aoshima, and Y. Tsuchiya. Opt. Lett. **27**, 309 (2002).
35. N. Aközbek, C.M. Bowden, A. Talebpour, and S.L. Chin. Phys. Rev. E, **61**, 4540 (2000).
36. O.G.Kosareva, V.P. Kandidov, A. Brodeur, and S.L. Chin. J. Nonlinear Opt. Phys. Mater. **6**, 485 (1997).
37. A. Chiron, B. Lamoroux, R. Lange, J.-F. Ripoche, M. Franco, B. Prade, G. Bonnaud, G. Riazuelo, and A. Mysyrowicz. Eur. Phys. J. **D6**, 383 (1999).
38. A. Talebpour, S. Petit, and S.L. Chin. Opt. Commun. **171**, 285 (1999).
39. W. Liu, Q. Luo, and S.L. Chin. Chin. Opt. Lett. **1**, 56 (2003).
40. V.I. Talanov. Sov. Phys. JETP Lett. **11**, 199 (1970).
41. W. Liu, J.-F. Gravel, F. Théberge, A. Becker, and S.L. Chin. Appl. Phys. B, **80**, 857 (2005).
42. F. Courvoisier, V. Boutou, J. Kasparian, E. Salmon, G. Méjean, J. Yu, and J.-P. Wolf. Appl. Phys. Lett. **83**, 213 (2003).
43. A.L. Gaeta. Phys. Rev. Lett. **84**, 3582 (2000).
44. N. Aközbek, M. Scalora, C.M. Bowden, and S.L. Chin. Opt. Commun. **191**, 353 (2001).
45. A. Talebpour, J. Yang, and S.L. Chin. Opt. Commun. **163**, 29 (1999). Corrections to this reference: There are two printing errors in this paper. In eq. (2) Z should read Z_{eff}, and in eq. (8) W_m should be w_m. The $\times$ sign should be omitted.
46. M. Kolesik, G. Katona, J.V. Moloney, and E.M. Wright. Appl. Phys. B, **77**, 185 (2003).
47. J. Kasparian, R. Sauerbrey, D. Mondelain et al. Opt. Lett. **25**, 1397 (2000).
48. O.G. Kosareva, V.P. Kandiddov, A. Brodeur, C.Y. Chien, and S.L. Chin. Opt. Lett. **22**, 1332 (1997).
49. S.L. Chin, V. Francois, J.M. Watson, and C. Delisle. Appl. Opt. **31**, 3383 (1992).
50. A. Brodeur, F.A. Ilkov, and S.L. Chin. Opt. Commun. **129**, 193 (1996).
51. L. Bergé and A. Couairon. Phys. Plasmas, **7**, 210 (2000).
52. A. Couairon and L. Bergé. Phys. Plasmas, **7**, 193 (2000).
53. P. Sprangle, J.R. Peñano, and B. Hafizi. Phys. Rev. E, **66**, 046418 (2002).
54. J. Muth-Böhm, A. Becker, and F.H.M. Faisal. Phys. Rev. Lett. **85**, 2280 (2000).
55. A.D. Bandrauk, S. Chelkowski, and I. Kawata. Phys. Rev. A, **67**, 013407 (2003).
56. A. Becker and F.H.M. Faisal. J. Phys. B, **38**, R1 (2005).
57. L.V. Keldysh. Sov. Phys. - JETP, **20**, 1307 (1965).

58. F.H.M. Faisal. J. Phys. B, **6**, L89 (1973).
59. H.R. Reiss. Phys. Rev. A, **22**, 1786 (1980).
60. A. Becker, L. Plaja, P. Moreno, M. Nurhuda, and F.H.M. Faisal. Phys. Rev. A, **64**, 023408 (2001).
61. J. Muth-Böhm, A. Becker, S.L. Chin, and F.H.M. Faisal. Chem. Phys. Lett. **337**, 313 (2001).
62. N. Aközbek, A. Becker, M. Scalora, S.L. Chin, and C.M. Bowden. Appl. Phys. B, **77**, 177 (2003).
63. D. Anderson. Phys. Rev. A, **27**, 3135 (1983).
64. M. Desaix, D. Anderson, and M. Lisak. JOSA B, **8**, 2082 (1991).
65. S. John and N. Aközbek. Phys. Rev. Lett. **71**, 1168 (1993).
66. T. Brabec and F. Krausz. Phys. Rev. Lett. **78**, 3282 (1997).
67. H. Nishioka, W. Odajima, K. Ueda, and H. Takuma. Opt. Lett. **20** 2505 (1995).
68. S. Chi and Q. Guo. Opt. Lett. **20**, 1598 (1995).
69. G. Fibich and B. Ilan. Opt. Lett. **26**, 840 (2001).
70. G. Fibich and B. Ilan. Physica D, **157**, 112 (2001).
71. S.L. Chin, A. Talebpour, J. Yang, S. Petit, V.P. Kandidov, O.G. Kosareva, and M.P. Tamarov. Appl. Phys. B, **74**, 67 (2002).
72. S.L. Chin, S. Petit, W. Liu, A. Iwasaki, M.-C. Nadeau, V.P. Kandidov, O.G. Kosareva, and K.Yu. Andrianov. Opt. Commun. **210**, 329 (2002).
73. V.I. Bespalov and V.I. Talanov. Sov. Phys. JETP Lett. **3**, 307 (1966).
74. S.A. Hosseini, Q. Luo, B. Ferland, W. Liu, S.L. Chin, O.G. Kosareva, N.A. Panov, N. Aközbek, and V.P. Kandidov. Phys. Rev. A, **70**, 033802 (2004).
75. Q. Luo, S.A. Hosseini, W. Liu et al. Appl. Phys. B, **80**, 35 (2005).
76. M. Mlejnek, M. Kolesik, J.V. Moloney, and E.M. Wright. Phys. Rev. Lett. **83**, 2938 (1999).
77. N. Aközbek, C.M. Bowden, and S.L. Chin. J. Mod. Opt. **49**, 475 (2002).
78. S. Tzortzakis, L. Bergé, A. Couairon, M. Franco, B. Prade, and A. Mysyrowicz. Phys. Rev. Lett. **86**, 5470 (2001).
79. L. Bergé, S. Skupin, F. Lederer et al. Phys. Rev. Lett. **92**, 225002 (2004).
80. L. Bergé, S. Skupin, G. Méjean, J. Kasparian, J. Yu, S. Frey, E. Salmon, and J.P. Wolf. Phys. Scr. **T107**, 135 (2004).
81. A. Dubietis, G. Tamošauskas, G. Fibish, and B. Ilan. Opt. Lett. **29**, 1126 (2004)
82. S. Carrasco, S. Polyakov, H. Kim, L. Jankovic, and G. Stegeman. Phys. Rev. E, **67**, 046616 (2003).
83. W. Liu, S.A. Hosseini, Q. Luo, B. Ferland, S.L. Chin, O.G. Kosareva, N.A. Panov, and V.P. Kandidov. New J. Phys. **6**, 6 (2004).
84. H. Wille, M. Rodriguez, J. Kasparian, D. Mondelain, J. Yu , A. Mysyrowicz, R. Sauerbrey, J.P. Wolf, and L. Woste. Eur. Phys. J. Appl. Phys. **20**, 183 (2002).
85. S.L. Chin and K. Miyazaki. Jpn. J. Appl. Phys. **38**, 2011 (1999).
86. H. Pépin, D. Comtois, F. Vidal et al. Phys. Plasmas, **8**, 2532 (2001).
87. J.F. Gravel, Q. Luo, D. Boudreau, X.P. Tang, and S.L. Chin. Anal. Chem. **76**, 4799 (2004).
88. Q. Luo, W. Liu, and S.L. Chin. Appl. Phys. B, **76**, 337 (2003).
89. N. Aközbek, A. Iwasaki, A. Becker, M. Scalora, S.L. Chin, and C.M. Bowden. Phys. Rev. Lett. **89**, 143901 (2002).
90. F. Théberge, N. Aközbek, W. Liu, J.F. Gravel, and S.L. Chin. Opt. Commun. **245**, 399 (2005).
91. F. Théberge, W. Liu, Q. Luo, and S.L. Chin. Appl. Phys. B, **80**, 221 (2005).
92. A. Proulx, A. Talebpour, S. Petit, and S.L. Chin. Opt. Commun. **174**, 305 (2000).
93. S. Tzortzakis, G. Méchain, G. Patalano et al. Opt. Lett. **27**, 1944 (2002).
94. S. Tzortzakis, B. Prade, M. Franco, A. Mysyrowicz, S.Hüller, and P. Mora. Phys. Rev. E, **64**, 057401 (2001).
95. F. Vidal, D. Comtois, C.Y. Chien et al. IEEE Trans. Plasma Sci. **28**, 418 (2000).
96. M. Rodriguez, R. Sauerbrey, H. Wille et al. Opt. Lett. **27**, 772 (2002).
97. D. Comtois, H. Pépin, F. Vidal et al. IEEE Trans. Plasma Sci. **31**, 377 (2003).
98. D. Comtois, H. Pépin, F. Vidal et al. IEEE Trans. Plasma Sci. **31**, 387 (2003).
99. A. Brodeur and S.L. Chin. Phys. Rev. Lett. **80**, 4406 (1998).
100. A. Brodeur and S.L. Chin. J. Opt. Soc. Am. B, **16**, 637 (1999).
101. P.K. Kennedy. IEEE J. Quantum Electron. **31**, 2241 (1995).
102. P.K. Kennedy, S.A. Boppart, D.X. Hammer, B.A. Rockwell, G.D. Noojin, and W.P. Roach. IEEE J.

Quantum Electron. **31**, 2250 (1995).
103. Yu.P. Raizer. Gas discharge physics. Springer-Verlag, New York. 1991.
104. D. Du, X. Liu, G. Korn, J. Squier, and G. Mourou. Appl. Phys. Lett. **64**, 3071 (1994).
105. W. Liu, O. Kosareva, I.S. Golubtsov, A. Iwasaki, A. Becker, V.P. Kandidov, and S.L. Chin. Appl. Phys. B, **76**, 215 (2003).
106. Q. Feng, J.V. Moloney, A.C. Newell, E.M. Wright, K. Cook, P.K. Kennedy, D.X. Hammer, B.A. Rockwell, and C.R. Thompson. IEEE J. Quantum Electron. **33**, 127 (1997).
107. M. Young and M. Hercher. J. Appl. Phys. **38**, 4393 (1967).
108. W. Liu, S.L. Chin, O.G. Kosareva, I.S. Golubtsov, and V.P. Kandidovd. Opt. Commun. **225**, 193 (2003).
109. H. Schroeder and S.L. Chin. Opt. Commun. **234**, 399 (2004).
110. H. Schroeder, M. Wagner, S. Kaesdorf, and K.L. Kompa. Ber. Bunsen Phys. Chem. **97**, 1688 (1993).
111. H. Schroeder, M. Wagner, and S. Kaesdorf. *In* Excimer lasers. *Edited by* L.D. Laude. Kluwer Academic Publication, New York. 1994. pp. 153–164.
112. S.S. Mao, F. Quere, S. Guizard, X. Mao, R.E. Russo, G. Petite, and P. Martin. Appl. Phys. A, **79**, 1695 (2004).
113. M.R. Kasaai, S. Lagacé, D. Boudreau, E. Förster, B. Müller, and S.L. Chin. J. Non-Cryst. Solids, **292**, 202 (2001).
114. M.R. Kasaai, V. Kacham, F. Théberge, and S.L. Chin. J. Non-Cryst. Solids, **319**, 129 (2003).
115. V. Koubassov, J.F. Laprise, F. Théberge, E. Förster, R. Sauerbrey, B. Müller, U. Glatzel, and S.L. Chin. Appl. Phys. B, **79**, 499 (2004).
116. K.M. Davis, K. Miura, M. Sugimoto, and K. Hirao. Opt. Lett. **21**, 1729 (1996).
117. N.T. Nguyen, A. Saliminia, W. Liu, S.L. Chin, and R. Vallée. Opt. Lett. **28**, 1591 (2003).
118. N.T. Nguyen, A. Saliminia, S.L. Chin, and R. Vallée. Proc. SPIE, **5578**, 665 (2004).
119. J. Kasparian, J. Solle, M. Richard, and J.P. Wolf. Appl. Phys. B, **79**, 947 (2004).
120. A. Dubietis, E. Gaižauskas, G. Tamošauskas, and P.D. Trapani. Phys. Rev. Lett. **92**, 253903 (2004).
121. H. Yang, J. Zhang, Y. Li, J. Zhang, Z. Chen, H. Teng, Z. Wei, and Z. Sheng. Phys. Rev. E, **66**, 016406 (2002).
122. X. Mao, S.S. Mao, and R.E. Russo. Appl. Phys. Lett. **82**, 697 (2003).
123. Q. Sun, H. Jiang, Y. Liu, Z. Wu, H. Yang, and Q. Gong. Opt. Lett. **30**, 320 (2005).
124. G. Méchain, A. Couairon, Y.-B. André, C. D'Amico, M. Franco, B. Prade, S. Tzortzakis, A. Mysyrowicz, and R. Sauerbrey. Appl. Phys. B, **79**, 379 (2004).
125. V.P. Kandidov, N. Akozbek, M. Scalora, O.G. Kosareva, A.V. Nyakk, Q. Luo, S.A. Hosseini, and S.L. Chin. Appl. Phys. B, **80**, 267 (2005).
126. L. Bergé, S. Skupin, G. Méjean, J. Kasparian, J. Yu, S. Frey, E. Salmon, and J.P. Wolf. Phys. Rev. E, **71**, 016602 (2005).
127. S.A. Trushin, S. Panja, K. Kosma, W.E. Schmid, and W. Fuß. Appl. Phys. B, **80**, 399 (2005).
128. X.P. Tang, A. Becker, W. Liu, M. Sharifi, O. Kosareva, V.P. Kandidov, P. Agostini, and S.L. Chin. Appl. Phys. B, **80**, 547 (2005).
129. X.P. Tang, A. Becker, W. Liu, M. Sharifi, O. Kosareva, V.P. Kandidov, P. Agostini, and S.L. Chin. Phys. Rev. A, **71**, 045451 (2005).
130. S. Champeaux and L. Berge. Phys. Rev. E, **68**, 066603 (2003).
131. N.L. Wagner, E.A. Gibson, T. Popmintchev, I.P. Christov, M.M. Murnane, and H.C. Kapteyn. Phys. Rev. Lett. **93**, 173902 (2004).